Asbestiform sepiolite coated by aliphatic hydrocarbons from Perletoa, Aosta Valley Region (Western Alps, Italy): characterization, genesis and possible hazards

Asbestiform sepiolite coated by aliphatic hydrocarbons from Perletoa, Aosta Valley Region (Western Alps, Italy): characterization, genesis and possible hazards

R. GIUSTETTO*[1,2], K. SEENIVASAN[2], E. BELLUSO[1,2,3]

[1]Department of Earth Sciences, University of Turin, via Valperga Caluso 35, 10125 Torino (Italy)
[2]NIS Centre (Nanostructured Interfaces and Surfaces), via Quarello 11, 10135 Torino (Italy)
[3]CNR, Institute of Geosciences and Earth Resources, via Valperga Caluso 35, 10125 Torino (Italy)

Corresponding author e-mail: roberto.giustetto@unito.it

Abstract

An atypical asbestiform sepiolite occurrence with exceptionally long fibres wrapped by a sheath of aliphatic hydrocarbons was found in the Gressoney Valley (Italian Western Alps) while monitoring asbestos presence in outcropping serpentinite rocks. Microscopic and FT-IR analyses proved that these fibres, apparently up to several cm long, are formed by bundles of thinner fibrils (average length: 150 μm) potentially dispersible in the environment. When observed with TEM these fibrils show a rhomboidal to parallelogram cross section (< 1 μm), whose surfaces are mostly covered by an aliphatic hydrocarbons film – an association never reported in literature. The sepiolite fibrils and their organic coating probably originated in sequential steps from precipitation of Si/Mg rich hydrothermal fluids, resulting from serpentinization of olivine and clinopyroxene, and Fischer-Tropsch-type reaction. Presence of hydrocarbons implies serious consequences on the sepiolite habit, as the organic wrap interacts with the fibrils surface reducing the amount of adsorbed water and favouring fragmentation of thicker units into thinner ones, due to an 'opening' process implying separation along *z* and cleavage on (110). This defibrillation mechanism, coupled to the extraordinary length, further increases these fibrils aspect ratio (length/width >> 3) thus amplifying their potential danger for human health when air dispersed and breathed.

Keywords: sepiolite, aliphatic hydrocarbons, Fischer-Tropsch-type reaction, hydrothermal system, noxiousness hazard.

1. Introduction

Sepiolite is a fibrous, trioctahedral phillosilicate clay mineral belonging to the palygorskite-sepiolite group. Its natural deposits occur as chemical sediments or reconstituted former sedimentary clays in epicontinental and inland seas and lakes, where somewhat saline groundwater discharges under semi-arid climatic conditions (Eugster and Hardie, 1975; Mayayo *et al*., 1998). Other sepiolite occurrences form by hydrothermal alteration of basaltic glass, volcanoclastic sediments or previous clays in the open ocean (in association with fore-arc basins and ocean ridges) or in calcareous soils by direct crystallization (Galán and Pozo, 2011). An authigenic clay mineral, sepiolite can form *in situ* through direct precipitation from solutions containing dissolved ionic species (namely Si and Mg; Trauth, 1977; Jones and Galan, 1988; Weaver, 1984) either in lacustrine (Chahi *et al*., 1997) or perimarine (Velde, 1985) environments in conditions of high alkalinity (pH: 8 - 9.5) and medium salinity. Direct precipitation from low-temperature hydrothermal solutions in continental environments were described (Imai and Otsuka, 1984) as well as precipitation, on or below the sea floor, from Mg/Si enriched low T (< 100°C) solutions formed by the interaction of ultramafic rocks with seawater circulating in the crust, particularly in transform zones (Bonatti *et al*., 1983). Other peculiar findings included possible biogenic origin induced by microorganisms (Leguey et al., 2010; Cuevas *et al*., 2012). Although not a common mineral, sepiolite deposits can be found worldwide – especially in Spain (Neogene

lacustrine sequences of the Madrid basin; Brell et al., 1985; Ordoñez *et al*., 1991) and Turkey (continental lacustrine deposits of the Ezkisehir Basin; Ece and Çoban, 1994), but also USA (Amargosa Desert deposit), Kenia and Tanzania (Amboseli deposit), China (Guanshan deposit), Greece (Ventzia basin deposit) and Somalia (El Bur deposit) (Galán and Pozo, 2011).

Sepiolite has various and useful industrial applications such as lubricant, catalyst, adsorbent, cleaning compress for restoration and cat litter (Àlvarez *et al*., 2011; Lòpez-Galindo *et al*., 2011). In addition sepiolite may be used as an asbestos substitute in building and seal materials, friction compounds for automotive brakes and high temperature insulators (Noda *et al*., 2009; Solebello, 2009) due to its habit and modest fibre length. Almost all commercially sold specimens have fibres < 5 μm long – the threshold of non-carcinogenicity accepted by the International Agency for Research on Cancer, World Health Organization (1997) – sometimes as the result of preliminary grinding. However, sepiolite occurrences from all over the world show high variability in cristallinity, fibre length and texture (Suárez and García-Romero, 2012; García-Romero and Suárez, 2013); samples with unusually long fibres (> 10 μm) were seldom identified and signalled for their carcinogenic potential (Pott *et al*., 1990; Pott *et al*., 1991; Bellman *et al*., 1997).

The structure of sepiolite [crystal-chemical formula $Mg_8Si_{12}O_{30}(OH)_4(OH_2)_4 \bullet 8H_2O$, s.g. Pbmn], first discussed by Preisinger (1959, 1963) and Brindley (1959), show a continuous waving tetrahedral sheet (T) alternated (along *X*) to a discontinuous octahedral one (O) forming ribbons elongated in the *Z*-axis direction. Such an arrangement, described as a framework of chessboard connected TOT ribbons (Ferraris *et al*., 2008), causes the structure to be crossed by *Z*-elongated tunnels (10.6 x 3.7 Å)

filled by weakly bound zeolitic H_2O and exchangeable ions. Tightly bound structural OH_2 (Bailey *et al*., 1980; Guggenheim and Krekeler, 2011) completes the coordination of Mg ions at the borders of the O ribbons, The structure of sepiolite differs from that of palygorskite, although recently intermediate forms were described which suggest the possible existence of a continuous compositional variation between the end-members of the group (Garcia-Romero *et al*., 2007; Garcìa-Romero and Suarez, 2010).

This study describes an atypical occurrence of sepiolite from Perletoa village, in the Gressoney Valley near the town of Aosta (Western Alps, Italy), showing unusually long fibres wrapped by a sheath of aliphatic hydrocarbons. The finding of asbestiform sepiolite in NW Italian outcropping rocks is not a novelty. Long fibre samples were detected in specific areas of the Valle d'Aosta, Piemonte and Liguria Regions (Belluso and Sandrone, 1989; Belluso *et al*., 1995). The genesis of organic matter (OM)-bearing clays (i.e. black shales or bituminous rocks) was reported from different sedimentary settings (Emeis and Weissert, 2009) or by weathering of mafic to ultramafic lithologies (Dos Anjos *et al*., 2010). Besides, hydrocarbon bearing clays were discovered in some metasomatized oxide-rich gabbros (Ciliberto *et al*., 2009) or in a diapiric intrusion in a diatremic tuff-breccia deposit, precipitated from a mixture of hot Si-rich hydrothermal fluids (350-400° C) and cold seawater (Manuella *et al*., 2012). Though sepiolite traces were detected in the latter study, no mention of its coupling to aliphatic hydrocarbons has ever been made so far. This work focuses therefore on such a peculiar association and consequent interaction, which affects the clay mineral habit possibly increasing its potential noxiousness for human health in case its fibres are airborne and breathed in large amounts.

2. Experimental

1.1 Materials and geological setting

The site of collection of the investigated sepiolite is located near Perletoa village, in the Gressoney Valley near the town of Aosta (Aosta Valley Region, Western Alps, Italy; 45° 48' 5" N, 7° 49' 25" E) (Fig. 1). This clay mineral was noted during systematic sampling to evaluate presence of asbestos and asbestiform minerals in massive to foliated serpentinite rocks from the main ultramafic bodies of the Italian Western Alps (Belluso *et al*., 1995). The analyzed sepiolite specimen was collected in the area of the Combin Zone (Geological Map of Aosta Valley, available at http://geonavsct.partout.it/pub/GeoNavSCT/index.html?repertorio=carta_geologica_100k), from a small serpentinitic lens outcropping (as peridotite, prasinite, amphibolite and eclogite lenses) in dominant calcschists.

(INSERT FIGURE 1)

2.2 Methods

Scanning electron microscopy (SEM) observations were obtained with a FEG SEM JEOL JSM6320F instrument and a SEM Stereoscan 360, Cambridge Instrument. The samples, coated by a 50 Å thick Au layer to allow conductivity, were attached to step brass stubs to allow examination of the fibres. Chemical characterization was performed by electron probe microanalysis (EPMA) using an EDS Link Pentafet, Oxford instrument. Due to the difficulties in analyzing fibrous samples, analyses were collected

on 10 x 10 μm^2 areas on a pressed, sintered and carbon-coated sepiolite pellet obtained with a press designed to prepare samples for infrared spectroscopy (operating conditions: 50 s counting time, 15 kV accelerating voltage, 25 mm working distance, 300 pA beam current). Collected data were processed with the Microanalysis Suite Issue 12, INCA Suite Version 4.01 and calibrated on natural mineral standards using the ZAF correction method. The weight% sums of oxides, showing no relevant heterogeneity, were averaged to obtain a reliable crystal-chemical formula.

A 120 kV transmission electron microscopy (TEM Philips CM12 working at 120 kV, LaB_6 filament, double tilt holder, equipped with an energy dispersive spectrometer EDAX Genesis 2000 System, TEM Quant Software PV8206/31 procession system) was used to examine crushed and ion thinned samples. Only medium to high TEM magnification can be performed at higher electron energy (lower ionisation), owing to the high instability of the fibrous sepiolite specimen under the electron beam. A TEM JEOL 2000FX (200 kV accelerating voltage, side entry, double-tilt ±30°, point-to-point resolution of 2.8 Å), equipped with a low-light camera (LHESA EM LH4086) with a YAG converter, was used. TEM specimens, cut perpendicular and parallel to the elongation of the fibres, were extracted from standard petrographic, uncovered thin sections (30-40 μm thick) embedded with epoxy resin and attached by Lakeside resin onto a glass slide. The microdrilled disks (attached to single-hole copper TEM slots) were thinned by ion beam milling (GATAN 600 Duomill working with Ar at room temperature, 5 kV and 0.50 mA per gun, 15° and finish angle of 12°). A powdered sample was ground in an agate and pestle mortar with isopropyl alcohol and then sonicated; two drops of the resulting suspension were deposited on a copper mesh grid previously coated with a 200 Å carbon film. At medium to high magnification, several

morphological and structural pictures were obtained. Selected area electron diffraction (SAED) were displayed but not photographed owing to very rapid fibres amorphization.

Thermogravimetric data were collected on a 15 mg sample with a simultaneous TGA/DSC SDT Q600, TA Instruments, in air flow with a heating rate of 10 °C min^{-1} from room temperature to 900 °C. DSC heat flow data were dynamically normalized using the instantaneous sample weight at any given temperature.

For infrared (IR) spectroscopy, the sepiolite was preliminarily activated in vacuum (pressure below $5*10^{-4}$ mbar) at room temperature, 120 and 150 °C for 1.5 hours each to progressively (and reversibly) remove the zeolitic H_2O. The resulting powder was used to make a pellet that was inserted in an IR cell and further heated in vacuum (pressure < $5*10^{-4}$ mbar) at 120 °C and 150 °C. IR absorption spectra were collected on a FTIR Bruker Vector 70, with a resolution of 2 cm^{-1} and collecting 64 scans for each spectrum. Data were collected at the different investigated *T* steps (room *T*, 120 and 150 °C) under controlled atmosphere.

For synchrotron X-ray powder diffraction (XRPD) and Rietveld refinement, the sepiolite specimen was initially purified by mechanically removing incidental macroscopic contaminants (serpentine, calcite and incidental pollutants) under the binocular stereo-microscope. The resulting fraction was dispersed in deionized water, thus possibly isolating the lighter suspended fraction from the heavier impurities [i.e. quartz and/or calcite] (Giustetto and Chiari, 2004). Massive purified samples were hand-ground in an agate mortar and crushed to powder. Conventional XRPD showed sepiolite to be the only detectable phase.

Synchrotron XRPD data were collected at room *T* at the European Synchrotron Radiation Facility (ESRF) in Grénoble (France), on the GILDA (*G*eneral-purpose

*I*talian beam-*L*ine for X-ray *D*iffraction and *A*bsorption) beamline, using a wavelength of λ = 0.6530 Å and Debye-Scherrer geometry. The specimen was loaded into a 1 mm diameter quartz-glass capillary to avoid preferred orientation. Collection time was 120 sec. Diffracted beams were collected with an area detector (MAR345) accessing d-values from 0.8 to 80 Å.

The GSAS software package (Larson and Von Dreele, 2007) and the EXPGUI graphical user interface (Toby, 2001) were used for Rietveld refinement. Background was fitted using a 14-term shifted-Chebyshev function and peak profiles modelled with a pseudo-Voigt function as parameterized by Thompson *et al*. (1987), with asymmetry corrections according to Finger *et al*. (1994). Initially, only the background, scale factor, zero and unit-cell parameters were refined. Later, fractional coordinates and occupancy factors for all atoms were refined, at first in alternate cycles (to minimize correlations) and then simultaneously. Soft constraints were imposed on tetrahedral and octahedral bond lengths and angles and progressively reduced. Isotropic displacement parameters (Uiso) for all atoms were adjusted using overall constraints for each chemical species. Preferred orientation for the (110) reflection (attenuated by data collection in capillary) was treated with the March-Dollase model (March, 1932; Dollase, 1986). Consistency of the refined structure was constantly checked through screening of the GOF (Goodness-Of-Fit) parameters, graphical fit between observed and calculated profiles and graphical representation of the refined model (Moldraw: Ugliengo *et al*., 1993). The lower soft-constraint weighting factor yielding reasonable bonds in tetrahedrons (F = 10) was kept to avoid unrealistic bond distances and polyhedrons distortions (Post *et al*., 2007; Post and Heaney, 2008; Giustetto *et al*., 2011a; Giustetto and Compagnoni, 2011).

3. **Results and discussion**

3.1 Macroscopic and stereomicroscopic observation

Even at the macroscopic scale, the asbestiform habit of the Perletoa sepiolite is evident. Long and apparently thick fibres (from 5 mm up to 7 cm), often grouped in bundles, can be observed even with the naked eye (V group: macroscopic fibres, after García-Romero and Suárez, 2013; Fig. 2).

(INSERT FIGURE 2)

These fibres are usually flexible (Fig. 2), with a cream to light brown colour, and readily split to thinner fibrils if manipulated. They usually crystallize parallel to the vein selvages (slip type), with thickness from < 1 mm to 1 cm. This morphology is common in the palygorskite-sepiolite group minerals, although massive, cardboard-like felts or 'mountain leather' (Grim, 1968; Frost *et al*., 1998; Imai and Otsuka, 2000) of tangled fibres forming an apparently continuous mat are also typical. Observations under the stereo-microscope showed that these long macroscopic fibres are bundles composed of many thinner fibrils, intricately intergrown and separable by mechanic stress.

3.2 Scanning, Transmission and Analytical Electron microscopy

SEM investigation showed that the bundles observed at the macroscopic scale or by optical stereomicroscope are composed of entangled, elongated and mainly parallel thinner fibrils, < 0,1 μm width and > 150 μm long (IV group: very long fibres, García-

Romero and Suárez, 2013). When mechanically stressed, these thinner units show great flexibility (Fig. 3).

(INSERT FIGURE 3)

Owing to their sensitivity to the electron beam after a few seconds of exposure these fibres degrade by losing crystallinity and habit. Thus, high-magnification images were impossible to obtain by TEM. SAED images from fibre sections showed rings relating to the different relative rotations of the fibres along their axis lengths. The brightness of the diffraction spots comes out in favour of at least a medium crystallinity degree, although other experimental parameters may also play a role. Low magnification TEM images of the sample thinned perpendicular to [001] (lengthening axis of the fibre bundle) show a large open texture, with spaces among the fibre bundles and sometimes even among the single primary units – or laths (interfibre or open porosity: García-Romero and Suárez, 2013; Fig. 4.a).

(INSERT FIGURE 4)

Fibre sections cut perpendicular to the bundle axis show nearly regular rhomboidal (thinner fibres) to parallelogram-like cross-sections (larger units, ‘parallelograms’ hereafter). Similarly oriented parallelograms are grouped in clusters; separate clusters show different orientations (Fig. 4.b). The parallelogram dimensions vary approximately between 150-750 (base) and 80-250 Å (height). Parallelograms with dimensions larger than those given above show an incipient ‘opening’ process (fibre separation), similar to the defibrillation observed in several sections of amphibole asbestos (e.g. Gunter *et al*., 2007). This ‘opening’ process causes fragmentation of larger into smaller parallelograms and occurs mainly along the traces of the (110) preferential cleavage plane (dashed white lines in Fig. 4.b). The separation starts mainly

from the fibre rim, deepening inside the core along a crankshaft direction which forms near 120° and 60° angles (Fig. 5). These parallelograms are not tightly aggregated as the global texture is characterized by medium to large interstitial spaces, sometimes larger than the parallelograms themselves, filled by an almost continuous thin film which, in some cases, apparently link the fibres. The film could not be characterized by electron probe microanalysis because of the very low analytical electron microscopy X-ray counts. This result suggests the presence of possible organic material, an assumption supported by FT-IR investigation (see paragraph 3.4). The film, located even in the smaller interstices (indicated by arrows in Fig. 4.b) suggests that it may be involved in the 'opening' process, favouring defibrillation and fibre separation of larger bundles into thinner fibrils (rods and/or laths: García-Romero and Suárez, 2013). These interstitial spaces, however, are not a consequence of beam damage to the sepiolite crystals because the parallelogram edges are clearly defined. A similar mechanism was recently described by Sciré et al. (2011), who observed how aliphatic hydrocarbons associated to flexible fibrous phyllosilicates (such as "serpentine") trigger defibrillation of bundles into primary units, producing an atypical foam-like texture.

(INSERT FIGURE 5)

TEM observations performed on sections parallel to the fibre axis are less significant, owing to the large number of fibrils along the thickness of the section (consequent to their small width) and their rapid damage under the electron beam. This observation indicates also the high degree of parallelism among fibrils.

The open channel defects (OCD) described by Krekeler and Guggenheim (2009) in a sepiolite specimen from Helsinki are less common here. These defects involve the

omission of single to multiple polysomes in a fibre (commonly four); sometimes multiple OCD appear in the same fibre, especially in the larger units (Fig. 4.b).

The chemical composition measured by SEM-EDS (Table 1) is consistent with previously published data (Suàrez and Garcia-Romero, 2011) and shows Si and Mg as the main components (as well as O and H), together with small amounts of Fe and Al substituting for Mg in octahedral coordination; Ca was also sporadically detected.

(INSERT TABLE 1)

On an anhydrous basis, the following crystal chemical formula was obtained: $Si_{12,18}O_{32}(Mg_{7,18},Fe_{0,29})_{\Sigma 7,47}$ (total iron as Fe^{3+}). The slight Si excess in tetrahedrons with respect to the ideal value (12) may be a result of small disseminated quantities of amorphous silica, sometimes reported in literature (Karakaya et al., 2011). This silica, undetected by XRPD and FT-IR, is probably a result of excess SiO_2 content dissolved in the circulating low-*T* hydrothermal fluids which presumably precipitated this sepiolite (see paragraph 3.6). A low octahedral content (i.e. < 8) is not uncommon in sepiolite owing to any trivalent iron and vacancies (Suàrez and Garcia-Romero, 2011).

3.3 Thermogravimetric analysis

(INSERT FIGURE 6)

Thermogravimetric (TGA) and heat flow (DSC) data collected on the Perletoa sepiolite (Fig. 6) are consistent with previous works (Nagy and Bradley, 1955; Brauner and Preisinger, 1956; Martin Vivaldi and Cano Ruiz, 1956; Caillère and Hénin, 1957; Preisinger, 1959; Hayashi *et al*., 1969; Nagata *et al*., 1974; Rautureau and Mifsud, 1977; Ruiz *et al*., 1996; Weir *et al*., 2002; Hubbard *et al*., 2003; Ovarlez *et al*., 2006,

2009). Although in sepiolite correlations between TGA features and structural changes are not straightforward nor partitioning among different kinds of water so strict (Mifsud *et al*., 1987), reasonable interpretations can be sketched. All main events and related attributions are detailed in Table 2.

(INSERT TABLE 2)

The weight loss recorded between room *T* and 110 °C (6.5 %), related to the release of superficially adsorbed water and less severely bound zeolitic H_2O, is slightly lower than that recorded in literature (i.e. about 10-11 %: Jones and Galan, 1988; Frost and Ding, 2003). This deficiency affects the hygroscopic rather than zeolitic H_2O content, as the roughly continuous organic film covering the fibres surface (see paragraph 3.2) probably limits the adsorption of physisorbed water. Loss of the 2nd half of structural OH_2, extending from 320 to 620 °C, is marked by no apparent signal in the derivative weight nor heat flow profiles (contrarily to Martin Vivaldi and Fenoll Hach-Ali, 1970 and Giustetto *et al*., 2011c) thus certifying the slow progression of such an event.

Combustion of hydrocarbons should give rise to an exothermic peak around 500° C (Sciré *et al*., 2011). Although a careful examination of the DSC profile reveals a weak exothermic hump around 470-480° C, no such an event is clearly observed here possibly due to the limited amounts of organic material forming the coating. The overall recorded weight loss (≅ 16.5 %) is slightly lower than that of other sepiolites (i.e. 18.5-19.5 %: Frost *et al*., 2009; Giustetto *et al*., 2011c), possibly as the result of the ascertained deficiencies in the hygroscopic H_2O content.

3.4 Fourier Transform IR spectroscopy

(INSERT FIGURE 7)

FT-IR spectra were collected on the Perletoa sepiolite in air at room *T* and in vacuum ($P < 5*10^{-4}$ mbar) upon heating at 120 and 150 °C, to eliminate contribution of the broad signals related to zeolitic H_2O. Data are consistent with previous works (Cannings, 1968; Hayashi *et al*., 1969; Mendelovici, 1973; Nagata *et al*., 1974; Prost, 1975; Mendelovici and Portillo, 1976; Post, 1978; Myriam *et al*., 1998; Frost *et al*., 2001; Jung and Grange, 2004; Ovarlez *et al*., 2009; Giustetto *et al*., 2010; Giustetto *et al*., 2011b; Bukas *et al*., 2013). Attribution of vibrational modes and related evolution with *T* rise are summarized in Table 3.

(INSERT TABLE 3)

The FT-IR spectrum collected in air at room *T* (pattern 1 in Figg. 7 and 8) is dominated by the broad signals related to both physisorbed and zeolitic H_2O, which mask the narrower bands of hydroxyls having stronger interactions. Weak but clearly visible vibrational modes can be appreciated in the 1350-1550 cm^{-1} region (at 1384 and 1509 cm^{-1}, separated by a broader hump at 1444 cm^{-1}; pattern 1 in Fig. 8, magnification; Table 3), where no bands of sepiolite should appear. These bands are consistent with those sometimes observed in literature on gabbroid or serpentinized/carbonated mantle-derived ultramafic xenoliths as well as saponite-rich clays originated from hydrothermal serpentinitic systems (Ciliberto *et al*., 2009; Sciré *et al*., 2011; Manuella *et al*., 2012) and attributed to δ(C–H) of saturated aliphatic hydrocarbons. Their presence can therefore be related to the organic film which fills the interstices among different fibres, possibly inducing the ‘opening’ of bigger parallelograms into thinner units as hinted by TEM (see Fig. 4.b, paragraph 3.2).

(INSERT FIGURE 8)

Evacuation at room *T* (pattern 2 in Figg. 7 and 8) causes loss of physisorbed and most zeolitic H_2O with disappearance of all related modes; conversely, all structural OH_2 is still preserved. This allows detection of weaker features at 3205, 2960, 2930 and 2854 cm^{-1} which represent the counterpart, in the stretching region, of those C–H modes related to aliphatic hydrocarbons (Silverstein *et al*., 2005; Sciré *et al*., 2011). The high intensity ratio between the 2930-2854 cm^{-1} signals [asymmetric and symmetric stretching of methylene (CH_2) groups respectively] and that at 2960 cm^{-1} [asymmetric stretching of methyl (CH_3) groups] indicates presence of hydrocarbons with long aliphatic chains (Coelho *et al*., 2006).

When evacuation is coupled to temperature rise, release of OH_2 is due to happen at lower *T* than in air. In the adopted vacuum conditions, loss of the 1st OH_2 half starts at 120 °C and proceeds until 175-200 °C (Serna *et al*., 1975; Giustetto *et al*., 2011b), causing structure folding (Preisinger, 1963; Serna *et al*., 1975, Post *et al*., 2007), reduction of the tunnel width and transformation from tetra- to di-hydrated sepiolite (SEP4H_2O and SEP2H_2O respectively; Ovarlez *et al*., 2011). Recent studies showed that these processes can be affected by incorporation of guest molecules in the tunnels, which prevents structure folding (Ovarlez *et al*., 2009, 2011; Giustetto *et al*., 2011b, 2012). Presence of the 3680 and 3674 cm^{-1} modes in the outgassed spectrum at 150 °C (pattern 4 in Fig. 7; Table 3) accounts for coexistence of folded and unfolded portions of the structure (Jung and Grange, 2004; Ovarlez *et al*., 2009). Furthermore, a broad signal appears at 3423 cm^{-1} which merits further discussion. A similar mode (3420 cm^{-1}) was reported by Giustetto *et al*. (2011b) in a sepiolite + indigo (2 wt %) composite heated at 150 °C in vacuum, and attributed to structural OH_2 perturbed by H-bonds with the incorporated dye. In the present study, the band tentatively result from unspecific

interactions existing between structural OH_2 at the tunnel edges and superficial grooves (Benli *et al*., 2012) and the almost continuous hydrocarbons film covering most fibrils. This suggestion is supported by the a similar signal in spectra collected on composite films between xylan-type hemicelluloses (polysaccharides) and fibrous sepiolite, indicative of H-bonding interactions (Sárossy *et al*., 2012).

Bands related to the hydrocarbons film covering the sepiolite fibres are basically unaltered by *T* rise, but tend to sharpen (curves 3 and 4 in Fig. 7). In the bending region a broad hump is observed at 1455 cm^{-1} bounded by sharper signals at 1509 and 1384 cm^{-1} (Fig. 8, magnification; Table 3).

3.5. Crystal structure refinement

Despite all inevitable limits due to fine grain size, modest crystallinity and fibrous habit, which cause the refinement of this highly defective clay mineral to be troublesome (Guggenheim and Krekeler, 2011), a structural model for the Perletoa sepiolite was proposed using the Rietveld method on powder synchrotron XRD data consistently with previous studies (Post *et al*., 2007; Giustetto *et al*., 2011a). Recently pioneering single-crystal XRD data were presented by Sanchez del Rio *et al*. (2011).

Initial fractional coordinates were taken from Giustetto *et al*. (2011a); only Mg was located in octahedral sites and small quantities of Ca in the tunnels were neglected. The low-angular position and asymmetry of the strong (110) reflection ($d_{110} \cong 12.2$ Å), bringing information about the channel content (Ovarlez *et al*., 2009), prevent its adequate fit so that in Rietveld procedures it is generally excluded (Chiari *et al*., 2003; Post *et al*., 2007; Post and Heaney, 2008; Giustetto *et al*., 2011a). The refinement was

first carried out in the 1.5– 41.5° 2θ range, including the strong (110) reflection, which was later excluded by maintaining the structural model refined so far.

(INSERT FIGURE 9)

(INSERT TABLE 4)

Fig. 9 shows the observed and calculated XRPD patterns of the Perletoa sepiolite and the related difference curve [magnification: patterns after exclusion of the (110) reflection]. Final refinement data, agreement factors and unit-cell parameters are listed in Table 4. Fractional coordinates, occupancy factors and displacement parameters for all atoms are reported in Table 5; the refined model is shown in Fig. 10.

(INSERT TABLE 5)

(INSERT FIGURE 10)

The goodness of fit is inevitably influenced by the disorder and multiple defects typical of these clay minerals (Giustetto and Chiari, 2004; Krekeler and Guggenheim, 2009), but the quality of the refined model is consistent with previous works (Artioli and Galli, 1994; Chiari *et al*., 2003; Post *et al*., 2007; Post and Heaney, 2008, Giustetto *et al*., 2011a). Although the relatively high standard deviations prevent an accurate discussion of the finer structural details, the unit cell shows an increase (0.03–0.05 Å) in the length of all parameters with respect to previous models (i.e. Post *et al*., 2007; Giustetto *et al*., 2011a), mostly along *y*, with consequent increase in the cell volume (≅ 1 %). The number of zeolitic H_2O molecules per unit cell (15.97) is in agreement with the ideal formula (16; Preisinger, 1959). Despite uncertainties remain about their sharp locations, these molecules are in sites consistent with those of Giustetto *et al*. (2011a); mutual O···O distances imply existence of a H-bond network (Jeffrey, 1997). The low

occupancy of ZW14 (Table 5) suggests that this molecule may alternatively occupy two close and equivalent sites.

3.6. Origin of aliphatic hydrocarbons and sepiolite genesis

The presence of hydrocarbons hosted in mafic to ultramafic, serpentinitic or gabbroic complexes involved in hydrothermal systems is well-known in literature (Charlou *et al*., 1998; Sciré *et al*., 2011). Hydrocarbons genesis can be either biotic or abiotic: the former involves biological processes including bacteriogenesis and thermogenesis (Schoell, 1988) whereas the latter is attributed to the Fischer-Tropsch-type (FT-t) reaction occurring in serpentinite-hosted hydrothermal systems (MacDonald and Fyfe, 1985; Konn *et al*., 2009). The FT-t reaction is an exothermic reduction of CO and CO_2 by gaseous H_2 catalyzed by group VIII metal ions (such as Fe, Co, Ni) or their oxides. The reactant C oxides mainly derive from mantle CO_2 dissolved in hydrothermal fluids (Charlou *et al*., 2002), whose concentration range from 3 to 20 mM. Furthermore, according to Ciliberto *et al*. (2009) CO_2 may be liberated during serpentinization of peridotitic olivine. In contrast, gaseous H_2 may be derived from the hydration of primary mafic minerals of peridotites (Marcaillou *et al*., 2011). Initially the FT-t reaction implies dissociation of the adsorbed CO with formation of an intermediate carbide, whose presence was detected in the early serpentinization products of peridotites (Pikovskii *et al*., 2004). Such an intermediate compound reacts with dissociated H_2 thus forming methane or higher hydrocarbons via insertion of $–CH_2–$ monomers in a growing Fischer-Tropsch chain (Schultz, 1999).

The collection site of the studied sepiolite specimen plots in the area of the Combin Zone, formed by dominant calcshists which locally contain clasts of metabasites, Mn-rich quartzites and massive to foliated serpentinite bodies locally occurring as metabreccias containing magnetite- or carbonate-rich levels (Gasco and Gattiglio, 2011). The Combin Zone is one of the two units – along with the Zermatt-Saas Zone – belonging to the Piedmont Zone which is part of the Piedmont-Ligurian basin of the Neo-Tethys ocean (Mahlen *et al*., 2005). This ocean spread during the Late Jurassic-Cretaceous (Piccardo *et al*., 2001), when its closure started and completed during the early Tertiary as a result of the European and African plates collision.

The Piedmont-Ligurian oceanic basin is represented by ophiolites exposed along the Western Alpine-Northern Appennine orogenic chain (Piccardo *et al*., 2001). A series of petrologic evidences supports the strong similarity of the Neo-Tethys ocean with ultra-spreading oceanic basins (e.g., Bach and Früh-Green, 2010) rather than with the traditional Penrose ophiolite model (Lagabrielle and Lemoine, 1997), such as:

i) the abundance of serpentinized spinel lherzolites intruded by gabbros;
ii) the MORB affinity of gabbros and basaltic vulcanites (Piccardo *et al*., 2001; Piccardo, 2008);
iii) the lack of sheeted dykes and gabbroic layer 3 and the very low volumes of gabbros and basalts.

Furthermore, Tethys ophiolites bear mineralogical assemblages attributed to hydrothermal processes (Manatschal and Müntener, 2009), including high-temperature (HT) hydrothermal alteration observed in mylonitized gabbros and serpentinization with formation of ophicalcites in serpentinized peridotites. Both processes resemble those observed in modern slow-spreading oceanic basin (e.g., Mid-Atlantic Ridge; Boschi *et*

al., 2006). Serpentinization primarily involves the complete alteration of olivine grains, whereas ortho- and clinopyroxenes are only occasionally preserved (Manatschal and Müntener, 2009). Ophicalcites, representing the *in situ* replacement of serpentine by calcite (Klein and Garrido, 2011), consist of clast- or matrix-supported breccias (Manatschal and Müntener, 2009) in which fragments of serpentinized peridotites are immersed in a matrix of red limestones and/or cemented by sparry calcite. The presence of ophicalcites provides evidence for hydrothermal activity at the Neo-Tethys seafloor at temperatures of 100-150 °C (Früh-Green *et al*., 1990). Carbonate precipitation occurs in modern seafloor due to circulation of alkaline (pH = 9-11) and Ca-rich fluids in serpentinite-hosted hydrothermal systems (Schroeder *et al*., 2002; Ribeiro da Costa *et al*., 2008; Bach and Früh-Green, 2010; Lavoie and Chi, 2010) or by oxidation of abiotic methane (Schwarzenbach *et al*., 2012). In addition, the finding of Mn-rich quartzites in the Tethys ophiolites has been interpreted by Tumiati *et al*. (2010) as a clear evidence for an oceanic hydrothermal origin of manganese ore deposits.

Serpentinite-hosted hydrothermal systems – analogous to those of the Combin Zone where the investigated sepiolite was collected – are ideal sites for the production of abiogenic hydrocarbons via the FT-t reaction, by means of progressive polymerization and polycondensation reactions (Konn *et al*., 2009; Taran *et al*., 2007). Since a widely accepted hypothesis for sepiolite genesis involves direct precipitation from an aqueous solution saturated with Mg and silica (Jones and Galán, 1988; Galán and Pozo, 2011) and with an insignificant Al activity (Birsoy, 2002), the Perletoa sepiolite probably originated from a similar process.

The absence of evident dolostones or dolomitic limestones sources in the area under study suggests that aqueous, low temperature (150-300 °C) hydrothermal fluids

probably derived Mg required to produce sepiolite by the weathering of surrounding serpentinized ultramafic rocks belonging to the nearby ocean-derived Piemonte Zone (Fig. 1). Si, Fe and Al were possibly provided by circulation of fluids extracted from serpentinites, as due to serpentinization of olivine and clinopyroxene (Augustin *et al*., 2008). Very small quantities of amorphous silica, whose presence can be assumed following crystal chemical formula calculations (see paragraph 3.2) and possibly due to a SiO_2 excess in these aqueous solutions, are expected to favour sepiolite precipitation (Birsoy, 2002).

The intimate association of the Perletoa sepiolite fibres with their aliphatic hydrocarbons sheaths of presumed abiogenic origin (an occurrence never reported before in literature) has therefore to be considered as the result of a complex hydrothermal process, which possibly generated both components in separate but sequential steps. The sheath of hydrocarbons, which occupies even the smaller interstitial spaces, limits the amount of adsorbable hygroscopic water and probably interacts with the fibres surface *via* specific bonds. These interactions, both mechanical and chemical, are expected to play a key-role in favouring defibrillation ('opening' process schematized in Fig. 5) of thicker bundles into thinner fibrous units (rods and/or laths). Consistently with the chronology proposed by Sciré *et al*. (2011) formation of sepiolite probably came first, due to crystal growth through the oriented aggregation of smaller subunits (laths) precipitated from Si/Mg rich fluids which gradually grouped into thicker bundles (García-Romero and Suárez, 2013). The abiotic genesis of hydrocarbons *via* FT-t reaction started later, thus allowing the covering of the bundles with a thin organic sheath. Mutual interactions between the hydrocarbon coating and the sepiolite fibres surface slowly but inexorably opened new interstices among the

different units, exposing new surfaces and promoting the beginning of the defibrillation process. The continuous production of hydrocarbons brought new organic matter to further slip into the formerly opened spaces, thus endorsing reiteration of the mechanism until discharge of primary sepiolite laths was reached.

The described phenomenon shows several analogies with Sherman (1970), who patented a protocol for defibrillating asbestos. An insoluble ethylenically unsaturated monomer was added to primary activated fibres dispersed in water (pH 4-5); its consequent polymerization formed an *in situ* organic coating on the surface of the asbestos fibrils. Such a method was aimed at obtaining a large number of primary fibrils, each coated by a polymer film, thus facilitating their dispersion in synthetic plastic compositions and reducing the tendency of such materials to crack or degrade after asbestos addition and mixing. It is curious to notice how such an artificial process, devised more than 40 years ago, has been mimicked by nature on an analogous material (this sepiolite occurrence, a potential asbestos substitute: see e.g., Kavas *et al*., 2004) by exploiting the coexistence of peculiar environmental conditions in a specific geological context.

4. Conclusions

The progressive defibrillation of the Perletoa sepiolite, triggered by the hydrocarbons sheath, not only causes a significant increase in the interfibre porosity (open texture) but also affects the fibre morphology enhancing its aspect ratio (length vs. thickness) from ‘high’ to ‘very high’. The thinner and exceptionally long fibrils

(rods and/or laths), therefore, potentially become more dangerous for human health due to their carcinogenic potential if dispersed in air and breathed in high doses.

However, it cannot be excluded that the hydrocarbons sheath could affect the surface reactivity of the sepiolite fibrils altering their chances of interacting with the pulmonary epithelium. For example, only the breathing of quartz particles with fresh surfaces increases the risk of lung damages due to their enhanced reactivity, whereas old and contaminated grains appear to be less dangerous (thus explaining why miners tend to be affected most; Schins *et al*., 2002; Albrecht *et al*., 2005). Besides, the toxicity of occasional exposure to aliphatic hydrocarbons *per se* (inhaled, skin absorbed or ingested) has already been acknowledged in literature (Farinha *et al*., 2011). Though the fibrous habit supposedly increases the risk, if the analogy holds then presence of this organic coating may enhance or else reduce this sepiolite noxiousness.

In the most recent report on the carcinogenic risks for humans caused by some silicates, the International Agency for Research on Cancer (IARC, 1997) stated that there is an "inadequate evidence in humans for the carcinogenicity of sepiolite"; despite this, a "limited evidence in experimental animals for the carcinogenicity of long sepiolite fibres" (length > 5 μm) was suggested. Fibres shorter than 5 μm, on the contrary, were considered harmless. On the whole, sepiolite fibres were included by IARC in "Group 3", meaning that further investigations are needed to evaluate their possible carcinogenicity or noxiousness (IARC, 2012). However, no data on sepiolite carcinogenicity for humans were available to the IARC working group in 1997, when the report was published. Data on the toxic effects for humans were concerned mostly for fibres < 4 μm. Realistically, the possible health issues of fibres characterized by exceptional lengths, such as those observed here, are not known.

Acknowledgements

The authors are indebted to Gabriele Ricchiardi for his precious help in collecting TGA data and to Silvia Bordiga for her invaluable hints about identification of aliphatic hydrocarbons.

Special thanks go to Simona Quartieri and Rossella Arletti for their support in collecting synchrotron XRPD diffraction patterns and to Alain Baronnet and Serge Nitsche for their valuable cooperation in collecting TEM data**.**

References

Albrecht, C., Knaapen, A.M., Becker, A., Höhr, D., Haberzettl, P., van Schooten, F.J., Borm, P.J., Schins, R.P. (2005) The crucial role of particle surface reactivity in respirable quartz-induced reactive oxygen/nitrogen species formation and APE/Ref-1 induction in rat lung. *Respiratory Research*, **6**(129), doi:10.1186/1465-9921-6-129.

Àlvarez, A., Santarén, J., Esteban-Cubillo, A. and Aparaicio P. (2011) Current industrial applications of palygorskite and sepiolite. Pp. 281-298 in: *Developments in palygorskite-sepiolite research, a new outlook on these nanomaterials* (E. Galan and A. Singer, editors). Elsevier B.V..

Artioli, G. and Galli, E. (1994) The crystal structures of orthorhombic and monoclinic palygorskite. *Material Science Forum*, **166**, 647-652.

Augustin, N., Lackschewitz, K.S., Kuhn, T., Dewey, C.W. (2008) Mineralogical and chemical mass changes in mafic and ultramafic rocks from the Logatchev hydrothermal field (MAR 15°N). *Marine Geology*, **256**(1-4), 18-29.

Bach, W. and Früh-Green, G.L. (2010) Alteration of the oceanic lithosphere and its implications for seafloor processes. *Elements*, **6**, 173-178.

Bailey, S.W., Alietti, A., Brindley, G.W., Formosa, M.L.L., Jasmund, K., Konta, J., Mackenzie, R.C., Nagasawa, K., Rausell-Colom, R.A. and Zvyagin, B.B. (1980) Summary of recommendations of AIPEA nomenclature committee. *Clays and Clay Minerals*, **28(1)**, 73-78.

Bellman, B., Muhle, H. and Ernst, H. (1997) Investigations on health-related properties of two sepiolite samples. *Environmental Health Perspectives*, **105(5)**, 1049-1052.

Belluso, E., Compagnoni, R. and Ferraris, G. (1995) Occurrence of asbestiform minerals in the serpentinites of the Piemonte Zone, Western Alps. Pp. 57-64 in: *Giornata di studio in ricordo del Prof. Stefano Zucchetti, Politecnico di Torino* (Politecnico di Torino, editor).

Belluso, E. and Sandrone, R. (1989) Occurrence of sepiolite in the marbles of the Dora Maira Massif (Italian Western Alps). *Miner. Petrogr. Acta*, **32**, 67-74

Benli, B., Du, H. and Celik, M.S. (2012) The anisotropic characteristics of natural fibrous sepiolite as revealed by contact angle, surface free energy, AFM and molecular dynamics simulation. *Colloids and Surfaces A: Physicochemical and Engineering Aspects*, **408**, 22-31.

Birsoy, R. (2002) Formation of sepiolite-palygorskite and related minerals from solution. *Clays and Clay Minerals*, **50**, 6, 736-745.

Bonatti, E., Craig Simmons, E., Breger, D., Hamlyn, P.R., Lawrence, J. (1983) Ultramafic rock/seawater interaction in the oceanic crust: Mg-silicate (sepiolite) deposit from the Indian Ocean floor. *Earth and Planetary Science Letters*, **62**(2), 229-238.

Boschi, C., Früh-Green, G.L., Delacour, A., Karson, J.A., Kelley, D.S. (2006) Mass transfer and fluid flow during detachment faulting and development of an oceanic core complex, Atlantis Massif (MAR 30°N). *Geochemistry, Geophysics, Geosystems*, **7**, doi: 10.1029/2005GC001074.

Brauner, K. and Preisinger, A. (1956) Structur und Enstehung des sepioliths. *Tschermaks Mineralogische und Petrographische Mitteilungen*, **6**, 1-2.

Brell, J.M., Doval, M., Caramés, M. (1985) Clay mineral distribution in the evaporitic Miocene sediments of the Tajo Basin, Spain. *Miner. Petrogr. Acta*, **29**-A, 267-276.

Brindley, G.W. (1959) X-ray and electron diffraction data for sepiolite. *American Mineralogist*, **44**, 495-500.

Bukas, V.J., Tsampodimou, M., Gionis, V., Chryssikos, G.D. (2013) Synchronous ATR infrared and NIR spectroscopy investigation of sepiolite upon drying. Vibrational Spectroscopy, **68**, 51-60.

Caillère, S. and Hénin, S. (1957) in: *The differential thermal investigation of clays* (R.C. Mackenzie, editor). Mineralogical Society, London.

Cannings, F.R. (1968) An Infrared study of hydroxyl groups in sepiolite. *Journal of Physical Chemistry*, **72**, 1072-1074.

Chahi, A., Fritz, B., Duplay, J., Weber, F., Lucas, J. (1997) Textural transition and genetic relationship between precursor stevensite and sepiolite in lacustrine sediments (Jbel Rhassoul, Morocco). *Clays Clay Min.*, **45**(3), 378-389.

Charlou, J.L., Fouquet, Y., Bougault, H., Donval, J.P., Etoubleau, J., Jean-Baptiste, P., Dapoigny, A., Appriou, P. and Rona, P.A. (1998) Intense CH_4 plumes generated by serpentinization of ultramafic

rocks at the intersection of the 15°20′N fracture zone and the Mid-Atlantic Ridge. *Geochimica et Cosmochimica Acta*, **62 (13)**, 2323–2333.

Charlou, J.L., Donval, J.P., Fouquet, Y., Jean-Baptiste, P., Holm, N. (2002) Geochemistry of high H_2 and CH_4 vent fluids issuing from ultramafic rocks at the Rainbow hydrothermal field, 36°14′N, MAR. *Chemical Geology*, **191**, 345–359.

Chiari, G., Giustetto, R. and Ricchiardi, G. (2003) Crystal structure refinements of palygorskite and Maya Blue from molecular modeling and powder synchrotron diffraction. *European Journal of Mineralogy*, **15**, 21–33.

Ciliberto, E., Crisafulli, C., Manuella, F.C., Samperi, F., Scirè, S., Scribano, V., Viccaro, M. and Viscuso E. (2009) Aliphatic hydrocarbons in metasomatized gabbroic xenoliths from Hyblean diametres (Sicily): genesis in a serpentinite hydrothermal system. *Chemical Geology*, **258**, 258-268.

Coelho, R.R., Hovell, I., de Mello Monte, M.B., Middea, A. and de Souza, A.L. (2006) Characterisation of aliphatic chains in vacuum residues (VRs) of asphaltenes and resins using molecular modelling and FTIR techniques. *Fuel Processing Technology*, **87**, 325-333.

Cuevas, J, Leguey, S., Ruiz, A.I. (2012) Evidence for the biogenic origin of sepiolite. Pp. 219-238 in: *Developments in palygorskite-sepiolite research, a new outlook on these nanomaterials* (E. Galan E. and A. Singer, editors). Elsevier B.V..

Dollase, W.A. (1986) Correction of intensities for preferred orientation in powder diffractometry: application of the March model. *Journal of Applied Crystallography*, **19**, 267-272.

Dos Anjos, C.W.D., Meunier, A., Guimaraès, E.M. and El Albani, A. (2010) Saponite-rich black shales and nontronite beds of the Permian Irati Formation: sediment sources and thermal metamorphism (Parana´ Basin, Brazil). *Clays and Clay Minerals*, **58**, 606-626.

Ece, Ö.I. and Çoban, F. (1994) Geology, occurrence and genesis of Eskişehir sepiolites, Turkey. *Clays and Clay Minerals*, **42**, 81-92.

Emeis, K.C. and Weissert, H. (2009) Tethyan_Mediterranean organic carbon-rich sediments from Mesozoic black shales to sapropels. *Sedimentology*, **56**, 247-266.

Eugster, H.P. and Hardie, L.A. (1975) Sedimenation in an ancient playa-lake complex: the Wilkins Peak member of the Green River Formation of Wyoming. *Bull. Geol. Soc. Am*., **86**, 319-334.

Farinha, A., Assunção, J., Vinhas, J. (2011) Renal toxicity of inhaled aliphatic hydrocarbons: a case report of chronic interstitial nephropathy. *Port J. Nephrol. Hypert*., **25(1)**, 43-46.

Ferraris, G., Makovicky, E. and Merlino, S. (2008) in: *Crystallography of modular materials*. Oxford, IUCr. Oxford University Press.

Finger, L.W., Cox, D.E. and Jephcoat, A.P. (1994) A correction for powder diffraction peak asymmetry due to axial convergence. *Journal of Applied Crystallography*, **27**, 892-900.

Frost, R.L., Cash, G.A. and Kloprogge, J.T. (1998) 'Rocky Mountain leather', sepiolite and attapulgite-an infrared emission spectroscopic study. *Vibrational Spectroscopy*, **16**, 173-184.

Frost, R.L. and Ding, Z. (2003) Controlled rate thermal analysis and differential scanning calorimetry of sepiolites and palygorskites. *Thermochimica Acta*, 397(1-2), 119-128.

Frost, R.L., Kristòf, J. Horvàth, E. (2009) Controlled rate thermal analysis of sepiolite. *Journal of Thermal Analysis and Calorimetry*, 98(3), 749-755.

Frost, R.L., Locos, O.B., Ruan, H. and Kloprogge, J.T. (2001) Near-infrared spectroscopic study of sepiolites and palygorskites. *Vibrational Spectroscopy*, **27**, 1-13.

Früh-Green, G.L., Weissert, H., Bernoulli, D. (1990) A multiple fluid history recorded in Alpine ophiolites. *Journal of the Geological Society of London*, **147**, 959-970.

Galán, E. and Pozo, M. (2011) Palygorskite and sepiolite deposits in continental environments. Description, genetic patterns and sedimentary settings. Pp. 131-135 in: *Developments in palygorskite-sepiolite research, a new outlook on these nanomaterials* (E. Galan E. and A. Singer, editors). Elsevier B.V..

García-Romero, E. and Suárez, M. (2013) Sepiolite-palygorskite: textural study and genetic considerations. *Applied Clay Science*, **86**, 129-144.

Garcia-Romero, E., Suarez, M., Santaren, J. and Alvarez, A. (2007) Crystallochemical characterization of the palygorskite and sepiolite from the Allou Kagne deposit, Senegal. *Clays and Clay Minerals*, **55**, 606-617.

Garcìa-Romero, E. and Suarez, M. (2010) On the chemical composition of sepiolite and palygorskite. *Clays and Clay Minerals*, **58**, 1-20.

Gasco, I. and Gattiglio, M. (2011) Geological map of the Upper Gressoney Valley. *Journal of Maps*, 6(1), 82-102.

Geological map of Aosta Valley, available on the official website of the Aosta Valley Region at http://geonavsct.partout.it/pub/GeoNavSCT/index.html?repertorio=carta_geologica_100k.

Giustetto, R. and Chiari, G. (2004) Crystal structure refinement of palygorskite from neutron powder diffraction. *European Journal of Mineralogy*, **16**, 521-532.

Giustetto, R., Seenivasan, K. and Bordiga, S. (2010) Spectroscopic characterization of a sepiolite-based Maya Blue pigment. *Periodico di Mineralogia*, Special Issue, 21-37.

Giustetto, R. and Compagnoni, R. (2011) An unusual occurrence of palygorskite from Montestrutto, Sesia-Lanzo Zone, internal Western Alps (Italy). *Clay Minerals*, **46**, 371-385.

Giustetto, R., Levy, D., Wahyudi, O., Ricchiardi, G. and Vitillo, J.G. (2011a) Crystal structure refinement of a sepiolite/indigo Maya Blue pigment using molecular modelling and synchrotron diffraction. *European Journal of Mineralogy*, **23**, 449-466.

Giustetto, R., Seenivasan, K., Bonino, F., Ricchiardi, G., Bordiga, S., Chierotti, M.R. and Gobetto, R. (2011b) Host/guest interactions in a sepiolite-based Maya Blue pigment: a spectroscopic study. *Journal of Physical Chemistry C*, **115**, 16764-16776.

Giustetto, R., Wahyudi, O., Corazzari, I. and Turci, F. (2011c) Chemical stability and dehydration behaviour of a sepiolite/indigo Maya Blue pigment. *Applied Clay Science*, **52**, 41-50.

Giustetto, R., Seenivasan, K., Pellerej, D., Ricchiardi, G. and Bordiga, S. (2012) Spectroscopic characterization and photo-thermal resistance of a hybrid palygorskite/methyl red Mayan pigment. *Microporous and Mesoporous Materials*, **155**, 167-176.

Grim, R.E. (1968) *Clay Mineralogy*. McGraw-Hill, New York.

Guggenheim, S. and Krekeler, M.P.S. (2011) The structure and microtextures of the palygorskite-sepiolite Group minerals. Pp. 15-16 in: *Developments in palygorskite-sepiolite research, a new outlook on these nanomaterials* (E. Galan and A. Singer, editors). Elsevier B.V..

Gunter, M.E., Belluso, E. and Mottana, A. (2007) Amphiboles: environmental and health concerns. Pp. 453-516 in: *Amphiboles: Crystal Chemistry, Occurrence and Heath Issues* (F.C. Hawthorne, R. Oberti, G., Della Ventura, A. Mottana, editors). Reviews in Mineralogy and Geochemistry, **67**, Mineralogical Society of America, Chantilly, Virginia.

Hayashi, H., Otsuka, R. and Imai, N. (1969) Infrared study of sepiolite and palygorskite on heating. *American Mineralogist*, **54**, 1613-1624.

Hubbard, B., Wenxing, K., Moser, A., Facey, G.A. and Detellier, C. (2003). Structural study of Maya Blue: textural, thermal and solid-state multinuclear magnetic resonance characterization of the palygorskite-indigo and sepiolite-indigo adducts. *Clays and Clay Minerals*, **51(3)**, 318–326.

Imai N. and Otsuka, R. (2000) Sepiolite and palygorskite in Japan. Pp. 211-232 in: *Palygorskite – sepiolite: occurrences, genesis and uses* (A. Singer and E. Galan, editors). *Developments in Sedimentology*, **37**.

International Agency for Research on Cancer, World Health Organization (1997) Sepiolite. Pp. 267-282 in: *IARC Monographs on the evaluation of carcinogenic risks to humans; Silica, some silicates, coal dust and para-aramid fibrils*. **68**, IARC Press.

International Agency for Research on Cancer, World Health Organization (2012) Arsenic, metals, fibres, and dusts. Pp. 501 in: *Monographs on the evaluation of carcinogenic risks to humans; A review of human carcinogens.* **100 C**, IARC Press.

Jeffrey, G.A. (1997) *An introduction to hydrogen bonding*, Oxford University Press.

Jones, B.F. and Galan, E. (1988) Palygorkite and sepiolite. Pp. 631-674 in: *Hydrous Phyllosilicates* (S.W. Bailey, editor), Reviews in Mineralogy, **19**. Mineralogical Society of America, Washington.

Jung, S.M.; Grange, P. (2004) Characterization of the surface hydroxyl properties of sepiolite and $Ti(OH)_4$ and investigation of new properties generated over physical mixture of $Ti(OH)_4$-sepiolite. *Applied Surface Science*, **221**, 167-177.

Karakaya, M.C., Karakaya, N., Temel, A. (2011) Mineralogical and geochemical characteristics and genesis of the sepiolite deposits at Polatli basin (Ankara, Turkey). *Clays and Clay Minerals*, **59(3)**, 286–314.

Kavas, T., Sabah, E., Celik, M.S. (2004) Structural properties of sepiolite-reinforced cement composite. *Cement and Concrete Research*, **34(11)**, 2135-2139.

Klein, F. and Garrido, C.J. (2011) Thermodynamic constraints on mineral carbonation of serpentinized peridotite. *Lithos*, **126**(3/4), 147-160.

Konn, C., Charlou, J.L., Donval, J.P., Holm, N.G., Dehairs, F., and Bouillon, S. (2009) Hydrocarbons and oxidized organic compounds in hydrothermal fluids from Rainbow and Lost City ultramafic-hosted vents. *Chemical Geology*, **258**, 299-314.

Krekeler, M.P.S. and Guggenheim, S. (2009) Defects in microstructure in palygorskite-sepiolite minerals: a transmission electron microscopy (TEM) study. *Applied Clay Science*, **39**, 98-105.

Lagabrielle, Y. and Lemoine, M. (1997) Alpine, Corsican, Apennine ophiolites: the slow-sreading ridge model. Ophiolites des Alpes, de Corse et des dorsales lentes. *Comptes Rendus de l'Académie des Sciences*, **325**, 909-920.

Larson, A.C. and Von Dreele, R.B. (2007) *GSAS – General Structure Analysis System*. Los Alamos National Laboratory Report No. LAUR 86-748.

Lavoie, D. and Chi, G. (2010) An Ordovician "Lost City" – venting serpentinite and life oases on lapetus seafloor. *Canadian J. Of Earth Sciences*, **47**, 199-207.

Leguey, S., Ruiz de Leòn, D., Ruiz, A.I., Cuevas, J. (2010) The role of biomineralization in the origino f sepiolite and dolomite. *Am. J. Sci*., **310**, 165-193.

Lòpez-Galindo, A., Viseras, C., Aguzzi, C., Cerezo, P. (2011) Pharmaceutical and cosmetic uses of fibrous clays. Pp. 299-324 in: *Developments in palygorskite-sepiolite research, a new outlook on these nanomaterials* (E. Galan and A. Singer, editors). Elsevier B.V..

Macdonald, A.H. and Fyfe, W.S. (1985) Rate of serpentinization in seafloor environments. *Tectonophysics*, **116**, 123-135.

Mahlen, N.J., Johnson, C.M., Baumgartner, L.P., Beard, B.L. (2005) Provenance of Jurassic Tethyan sediments in the HP/UHP Zermatt-Saas Ophiolite, Western Alps. *GSA Bull*., **117**(3/4), 530-544.

Manatschal, G. and Müntener, O. (2009) A type sequence across an ancient magma-poor ocean-continent transition: the example of the western Alpine Tethys ophiolites. *Tectonophysics*, **473**, 4-19

Manuella, F.C., Carbone, S. and Barreca, G. (2012) Origin of saponite-rich clays in a fossil serpentinite-hosted hydrothermal system in the crustal basement of the Hyblean plateau (Sicily, Italy). *Clays and Clay Minerals*, **60(1)**, 18-31.

Marcaillou, C., Muñoz, M., Vidal, O., Parra, T. and Harfouche, M. (2011) Mineralogical evidence for H_2 degassing during serpentinization at 300ºC/300 bar. *Earth and Planetary Science Letters*, **303**, 281-290.

March, A. (1932) Mathematische Theorie der Regelung nach der Korngestalt bei affiner Deformation. *Zeitschrift für Kristallographie*, **81**, 285-297.

Martin Vivaldi, J.L. and Cano Ruiz, J. (1956). Contribution to the study of sepiolite, III. The dehydration process and the types of water molecules. *Clays and Clay Minerals*, **4**, 177-180.

Martin Vivaldi, J.L. and Fenoll Hach-Ali, P. (1970) Palygorskite and sepiolite (Hormites). Pp. 553-573 in: *Differential thermal analysis* (R.M. Mackenzie, editor). Academic Press, London.

Mayayo, M.J., Torres-Ruiz, J., Gonzalez-Lopez, J.M., Lopez-Galindo, A., Bauluz, B. (1998) Mineralogical and Chemical characterization of the sepiolite/Mg-smectite deposit at Mara (Calatayud basin, Spain). *Eur. J. Miner*., **10**, 367-383.

Mendelovici, E. (1973) Infrared study of attapulgite and HCl treated attapulgite. *Clays and Clay Minerals*, **21**, 115-119.

Mendelovici, E. and Portillo, D.C. (1976) Organic derivatives of attapulgite-I. Infrared spectroscopy and X-ray diffraction studies. *Clays and Clay Minerals*, **24**, 177-182.

Mifsud, A., Garcia, I. and Corma, A. (1987) Thermal stability and textural properties of exchanged sepiolites. Pp. 392-394 in: *Proceedings Euroclay '87*. Sociedad Espanola de Arcilla, Sevilla.

Myriam, M., Suarez, M. and Martìn-Pozas, J.M. (1998). Structural and textural modifications of palygorskite and sepiolite under acid treatment. *Clays & Clay Minerals*, **46(3)**, 225-231.

Nagata, H., Shimoda, S. and Sudo, T. (1974) On dehydration of bound water in sepiolite. *Clays and Clay Minerals*, **22**, 285-293.

Nagy, B. and Bradley, W.F. (1955) The structural scheme of sepiolite. *American Mineralogist*, **40**, 885-892.

Noda, H., Miyagawa, K., Kobayashi, M., Horiguchi, H., Ozawa, K., Kumada, N., Yonesaki, Y., Takei, T. and Kinomura, N. (2009) Preparation of cordierite from fibrous sepiolite. *Journal of the Ceramic Society of Japan*, **117(11)**, 1236-1239.

Ordoñez, S., Calvo, J.P., Garcìa del Cura, M.A., Alonso Zarza, A.M., Hoyos, M. (1991) Sedimentology of sodium sulphate deposits and special clays from the Tertiary Madrid Basin (Spain). In: Anadòn, P., Cabrera, L.I., Keiths, K. (Eds.), *Lacustrine Facies Analysis*, *Spec. Publ. Int. Ass. Sediment*, vol. **13**, Blackwell Scientific Publications, Oxford, pp. 39-55.

Ovarlez, S., Chaze, A.M., Giulieri, F. and Delamare, F. (2006) Indigo chemisorption in sepiolite. Application to Maya Blue formation. *Comptes Rendu Chimie*, **9**, 1243-1248.

Ovarlez, S., Giulieri, F., Chaze, A.M., Delamare, F., Raya, J. and Hirschinger J. (2009). The incorporation of indigo molecules in sepiolite tunnels. *Chemistry A European Journal*, **15**, 11326-11332.

Ovarlez, S., Giulieri, F., Delamare, F., Sbirrazzuoli, N. and Chaze, A.M. (2011) Indigo-sepiolite nanohybrids: temperature-dependent synthesis of two complexes and comparison with indigo-palygorskite systems. *Microporous and Mesoporous Materials*, **142**, 371-380.

Piccardo, G.B. (2008) The Jurassic Ligurian Tethys, a fossil, ultraslow-spreading ocean; the mantle perspective. *Geol. Soc. London, Spec. Publ*., **293**, 11-34.

Piccardo, G.B., Rampone, E., Romairone, A., Scambelluri, M., Tribuzio, R., Beretta, C. (2001) Evolution of the Ligurian Tethys: inference from petrology and geochemistry of the Ligurian ophiolites. *Per. Mineral*., **70**(2), 147-192.

Pikovskii, Y.I., Chernova, T.G., Alekseeva, T.A. and Verkhovskaya, Z.I. (2004) Composition and nature of hydrocarbons in modern serpentinization areas in the ocean. *Geochemistry International*, **42**, 971–976.

Post, J.E. (1978) Sepiolite deposits of the Las Vegas, Nevada Area. *Clays and Clay Minerals*, **26**, 58-64.

Post, J.E., Bish, D.L. and Heaney P.J. (2007) Synchrotron powder X-ray diffraction study of the structure and dehydration behavior of sepiolite. *American Mineralogist*, **92**, 91-97.

Post, J.E. and Heaney, P.J. (2008) Synchrotron powder diffraction study of the structure and dehydration behavior of palygorskite. *American Mineralogist*, **93**, 667-675.

Pott, F., Bellman, B., Muhle, H., Rödelsperger, K., Rippe, R.M., Roller, M. and Rosenbruch, M. (1990) Intraperitoneal injection studies for the evaluation of the carcinogenicity of fibrous phyllosilicates. Pp. 319-329 in: *Health Related Effects of Phyllosilicates* (J. Bignon, editor). North Atlantic Treaty Organization Advanced Study Institute Series, Vol. G21, Ecological Sciences, Berlin West, Springer-Verlag.

Pott, F., Roller, M., Rippe, R.M., Germann, P.G. and Bellman, B. (1991) Tumors by the intraperitoneal and intrapleural routes and their significance for the classification of mineral fibres. Pp. 547-565 in: *Mechanisms in Fibre Carcinogenesis* (R.C. Brown, J.A. Hoskins and N.F. Johnson, editors). New York/London Plenum Press.

Preisinger, A. (1959) X-ray study of the structure of sepiolite. *Clays and Clay Minerals*, **6**, 61-67.

Preisinger, A. (1963) Sepiolite and related compounds: its stability and application. *Clays and Clay Minerals*, **10**, 365-371.

Prost, R. (1975) Infrared study of the interactions between the different kinds of water molecules present in sepiolite. *Spectrochimica Acta*, **31A**, 1497-1499.

Rautureau, M. and Mifsud, A. (1977) Etude par microscope electronique des differents etats d'hydratation de la sepiolite. *Clay Minerals*, **12**, 309–318.

Ribeiro da Costa, I., Barriga, F.J.A.S, Taylor, R.N. (2008) Late seafloor carbonate precipitation in serpentinites from the Rainbow and Saldanha sites (Mid-Atlantic-Ridge). *Eur. J. Min*., **20**(2), 173-181.

Ruiz, R., del Moral, J.C., Pesquera, C., Benito, I. and González, F. (1996) Reversible folding in sepiolite: study by thermal and textural analysis. *Thermochimica Acta*, **279**, 103–110.

Sanchez del Rio, M., Garcia-Romero, E., Suarez, M., da Silva, I., Fuentes Montero, L. and Martinez-Criado, G. (2011) Variability in sepiolite: Diffraction studies. *American Mineralogist*, **96**, 1443-1454.

Sárossy, Z., Blomfeldt, T.O.J., Hedenqvist, M.S., Bender Koch, C., Sinha Ray, S. and Plackett, D. (2012) Composite films of arabinoxylan and fibrous sepiolite: morphological, mechanical and barrier properties. *Applied Materials and Interfaces*, **4**, 3378-3386.

Schins, R.P., Duffin, R., Höhr, D., Knaapen, A.M., Shi, T., Weishaupt, C., Stone, V., Donaldson, K., Borm, P.J. (2002) Surface modification of quartz inhibits toxicity, particle uptake, and oxidative DNA damage in human lung epithelial cells. *Chemical Research in Toxicology*, 15(9), 1166-1173.

Schoell, M. (1988) Multiple origins of methane in the Earth. Chemical Geology, **71**, 1–10.

Schroeder, T., John, B., Frost, B.R. (2002) Geologic implication of seawater circulation through peridotite exposed at slow-spreading mid-ocean ridges. *Geology*, **30**, 367-370.

Schulz, H. (1999) Short history and present trends of Fischer–Tropsch synthesis. *Applied Catalysis A: General*, **186**, 3–12.

Schwarzenbach, E., Früh-Green, G.L., Bernasconi, S.M., Alt, J.C., Shanks, W.C., Gaggero, L., Crispini, L. (2012) Sulphur geochemistry of peridotite-hosted hydrothermal systems: comparing the Ligurian ophiolites with oceanic serpentinites. *Geochimica et Cosmochimica Acta*, **91**, 283-305.

Sciré, S., Ciliberto, E., Crisafulli, C., Scribano, V., Bellatreccia, F., Della Ventura, G. (2011) Asphaltene-bearing mantle xenoliths from Hyblean diatremes, Sicily. *Lithos*, **125**, 956-968.

Serna, C., Ahlrichs, J.L. and Serratosa, J.M. (1975) Folding in sepiolite crystals. *Clays and Clay Minerals*, **23**, 452-457.

Sherman, M.A. (1970). Coated asbestos and method of making and using same. United States Patent no. 3519594A, Lexington, Mass, assignor to Amicon Corporation, Lexington, Mass, a corporation of Massachusetts No Drawing. Filed Nov. 9, 1967, Ser. No. 681,933. Available at http://www.google.com/patents/US3519594.

Silverstein, R.M., Webster, F.X. and Kiemle, D.J. (2005) Spectroscopic Identification of Organic Compounds, 7th edition. John Wiley and Sons, New Jersey, USA.

Solebello L. (2009) Fibrous sepiolite use as an asbestos substitute: analytical basics. *Microscopy Today*, **15**, 18-19.

Suárez, M. and García-Romero, E. (2011) Advances in the Crystal Chemistry of Sepiolite and Palygorskite. Pp. 33-65 in: *Developments in Palygorskite-Sepiolite Research, a new outlook on these nanomaterials* (E. Galan and A. Singer, editors). Elsevier B.V..

Suárez, M. and García-Romero, E. (2012) Variability of the surface properties of sepiolite. *Applied Clay Science*, **67-68**, 72-82.

Taran, Y.A., Kliger, G.A. and Sevastianov, V.S. (2007) Carbon isotope effects in the open system Fischer–Tropsch synthesis. *Geochimica et Cosmochimica Acta*, **71**, 4474–4487.

Thompson, P., Cox, D.E. and Hastings, J.B. (1987) Rietveld refinement of Debye-Scherrer synchrotron data from Al_2O_3. *Journal of Applied Crystallography*, **20**, 79–83.

Toby, B.H. (2001) EXPGUI, a graphical user interface for GSAS. *Journal of Applied Crystallography*, **34**, 210-213.

Trauth, N. (1977) Argiles puaporitiques dans les sedimentation carbonatée et epicontinental tertiaire, Bassin de Paris, Mormoiron et Salenelles (France), Ibel Ghassoul (Maroc). *Sciences Géologiques Memoire*, **49**, pp. 195.

Tumiati, S., Martin, S., Godard, G. (2010) Hydrothermal origin of manganese in the high-pressure ophiolite metasediments of Praborna ore deposit (Aosta Valley, western Alps). *Eur. J. Min*., **22**, 577-594.

Ugliengo, P., Viterbo, D. and Chiari, G. (1993) MOLDRAW: molecular graphics on a personal computer. *Kristallographie*, **207**, 9.

Velde, B. (1985) Clay minerals: a physic-chemical explanation of their occurrences. In: *Developments in Sedimentology*, **40**, Elsevier, Nueva York, pp. 187-198.

Weaver, C.E. (1984) Origin and geologic implications of the palygorskite deposits of SE United States. In: Singer, A., Galàn, E. (Eds.), Palygorskite-Sepiolite: Occurrences, Genesis and Uses. *Developments in Sedimentology*, **37**, Elsevier, Amsterdam, pp. 39-58.

Weir, M.R., Kuang, W., Facey, G.A. and Detellier, C. (2002) Solid-state nuclear magnetic resonance study of sepiolite and partially dehydrated sepiolite. *Clays and Clay Minerals*, **50**, 240–247.

Table Captions

Table 1. Chemical composition (weight % oxides and mean value) and cations number calculated on anhydrous basis (32 oxygens) of the studied Perletoa sepiolite.

Table 2. TGA weight losses and related attributions for the Perletoa sepiolite.

Table 3. FT-IR active vibrational modes and related attributions at different temperatures and vacuum conditions for the Perletoa sepiolite and the superficial hydrocarbons sheath.

Table 4. Crystal-chemical formula, space group, cell parameters and refinement data for the Perletoa sepiolite.

Table 5. Refined fractional atomic coordinates, occupancy factors and isotropic displacement parameters for the Perletoa sepiolite.

Tables

Oxides (wt%)	1	2	3	4	5	6	7	8	9	10	11	12	13	Average
SiO_2	56.05	57.35	56.73	56.04	56.73	58.28	56.23	56.93	56.69	57.44	54.38	54.46	56.12	56(1)
Fe_2O_3	1.41	1.32	1.97	2.01	1.94	2.33	2	1.62	1.98	2.11	1.52	1.44	1.71	1.8(3)
MgO	22.13	22.67	22.25	22.11	22.84	23.38	22.14	22.36	21.87	23.37	21.39	21.9	21.74	22.3(6)
CaO	0	0	0	0.74	0	0	0	0	0	0	0	0	0	=
Σ	79.58	81.34	80.95	80.91	81.51	83.99	80.38	80.9	80.53	82.91	77.29	77.8	79.57	81(2)
Cations														
Si	12.23	12.24	12.20	12.11	12.13	12.11	12.18	12.22	12.24	12.08	12.22	12.17	12.25	12.18(6)
Fe^{3+}	0.23	0.21	0.32	0.33	0.31	0.36	0.33	0.26	0.32	0.33	0.26	0.24	0.28	0.29(5)
Mg	7.20	7.21	7.13	7.12	7.28	7.24	7.15	7.16	7.04	7.33	7.17	7.30	7.07	7.19(9)
Σ	19.66	19.66	19.65	19.56	19.72	19.71	19.66	19.64	19.60	19.74	19.65	19.71	19.60	19.66(5)
Ca	0	0	0	0.17	0	0	0	0	0	0	0	0	0	=

Table 1.

Temperature range (° C)	Weigth loss (%)	DSC event	Attribution and comments
25 – 110	6.5	endothermic (110° C)	Loss of physisorbed water and less severely bound zeolitic H_2O (tetra-hydrated sepiolite; SEP4H_2O)
120 – 310	3.5	endothermic (310° C)	Loss of residual zeolitic H_2O and 1st fraction of structural OH_2 (di-hydrated sepiolite; SEP2H_2O)
320 – 620	3.5	=	Loss of 2nd fraction of structural OH_2 (anhydrous sepiolite)
		endothermic (810° C)	(Possible) decarbonation of calcite traces
650 – 820	3.0	endothermic (830° C) exothermic (850° C)	Loss of framework OH (dehydroxylation) and transformation to clinoenstatite (or an amorphous phase)
Total	16.5		

Table 2.

Sepiolite				
Room *T* in air (cm^{-1})	**Room *T* in vacuum** ($5*10^{-4}$ mbar)	**120° C in vacuum** ($5*10^{-4}$ mbar)	**150° C in vacuum** ($5*10^{-4}$ mbar)	**Attribution and comments**
Stretching region (2750 - 3750 cm^{-1})				
3246	=	=	=	ν(OH) of physisorbed water, lost by evacuating at room *T*
3358	=	=	=	ν(OH) of zeolitic H_2O, lost by evacuating at room *T*
=	=	=	3423	Unspecific interactions of structural OH_2 (possibly with the aliphatic hydrocarbons sheath)
3568	3550	3550	3531	ν(OH) of structural OH_2; red-shift at 3550 and 3531 cm^{-1} are due to H-bond and symmetric ν(OH_2) variations
3623	3623	3623	3644-3603	ν(OH) of structural OH_2; splitting at 150° is due to variations in the antisymmetric and symmetric ν(OH_2)
3690	3680	3680	3680	ν(OH) of hydroxyl in O sheet; typical of unfolded sepiolite structure
=	=	=	3674	ν(OH) of hydroxyl in O sheet; accounts for intervened folding of the sepiolite structure
=	=	=	3692	H-H repulsion of framework hydroxyls (Mg-OH) due to approaching of residual OH_2 dislocated by structural folding
=	3719	3719	3719	ν(Si-OH); gradual intensity decay with *T* rise
=	=	3738	3738	ν(OH); perturbation of superficial silanols; Si-OH liberation at the edge of the O ribbons due to structure folding
Bending region (1400 - 1800 cm^{-1})				
1660	1623-1613	1623-1613	1625	δ(H_2O) phys./zeolitic (room *T*) - δ(OH_2) (vacuum/heat); intensity decay with *T* rise accounts for gradual OH_2 loss
1212	1193	1195	1198	δ(Si-O)

Aliphatic hydrocarbons				
Room *T* in air (cm^{-1})	**Room *T* in vacuum** ($5*10^{-4}$ mbar)	**120° C in vacuum** ($5*10^{-4}$ mbar)	**150° C in vacuum** ($5*10^{-4}$ mbar)	**Attribution and comments**
Stretching region (2750 - 3750 cm^{-1})				
=	3205	3205	3213	ν(C-H); slightly blue-shifts at 150° C
=	2960	2960	2960	ν(CH_3)
=	2930	2930	2930	ν(CH_2)
=	2854	2854	2854	ν(CH_2)
Bending region (1400 - 1800 cm^{-1})				
1384	1384	1384	1384	δ(CH_3) symmetric
=	=	1403	1403	δ(C-H); appears at 120° C
1444	1444	1455	1455	δ(CH_2) scissoring, δ(CH_3) asymmetric; blue-shifts at 120° C
1509	1509	1509	1509	δ(C-H)

Table 3.

Formula	$Si_{12,18}O_{32}(Mg_{7,18},Fe_{0,29})_{\Sigma 7,47}$
Space group	*Pncn*
a (Å)	13.442(2)
b "	27.072(3)
c "	5.2926(6)
V (Å^3)	1925.9(4)
$\Delta\rho_{min}$, $\Delta\rho_{max}$ (e/Å^3)	-0.300; 0.305
R	0.0202
R_{wp}	0.0271
R(F^2)	0.1260
reduced χ^2	8.420

Table 4.

Atom type	Label	*x*	*y*	*z*	Fraction	U_{iso}
Mg	Mg1	0	0.027(1)	0.25	1.00	0.008(2)
Mg	Mg2	0	0.089(1)	0.75	1.00	0.008(2)
Mg	Mg3	0	0.143(1)	0.25	1.00	0.008(2)
Mg	Mg4	0	0.204(1)	0.75	1.00	0.008(2)
O	O1	0.075(2)	0.024(1)	0.549(6)	1.00	0.016(3)
OH	O2	0.088(2)	0.082(2)	0.096(7)	1.00	0.016(3)
O	O3	0.076(2)	0.139(1)	0.588(6)	1.00	0.016(3)
Si	Si1	0.198(1)	0.0280(7)	0.578(4)	1.00	0.011(2)
Si	Si2	0.197(1)	0.1415(6)	0.582(4)	1.00	0.011(2)
Si	Si3	0.216(1)	0.1944(5)	0.080(4)	1.00	0.011(2)
O	O4	0.096(2)	0.204(1)	0.082(7)	1.00	0.016(3)
O	O5	0.245(2)	-0.001(1)	0.328(4)	1.00	0.016(3)
O	O6	0.238(2)	0.0849(8)	0.574(4)	1.00	0.016(3)
O	O7	0.246(2)	0.161(1)	0.317(5)	1.00	0.016(3)
O	O8	0.253(2)	0.171(1)	0.812(5)	1.00	0.016(3)
O	O9	0.25	0.25	0.137(8)	1.00	0.016(3)
OH_2	SW10	0.078(2)	0.2553(8)	0.572(7)	1.03(6)	0.025(7)
H_2O	ZW11	0.574(4)	-0.091(3)	0.034(9)	0.94(7)	0.10(4)
H_2O	ZW12	0.5	0.186(4)	0.25	0.76(9)	0.10(4)
H_2O	ZW13	0.5	0.013(3)	0.25	0.98(9)	0.10(4)
H_2O	ZW14	0.50(1)	0.168(4)	0.74(2)	0.19(4)	0.10(4)

Table 5.

Figure captions

Figure 1. Simplified tectonic sketch-map of the Western Alps. Helvetic Domain: Mont Blanc-Aiguilles-Rouges (MB); Penninic Domain: Grand Saint Bernard Zone (SB) and Internal Crystalline Massifs of Monte Rosa (MR), Gran Paradiso (GP), Dora-Maira (DM) and Valosio (V); Piemonte Zone of calcschists (light green) with meta-ophiolites (dark green): Lanzo Ultramafic Massif (LM); Austro-alpine Domain: Dent-Blanche nappe (DB), M. Emilius nappe (ME) and Sesia Zone (SZ); Southalpine Domain (SA); Nappe of Embrunais-Ubaye Flysch (EU); Canavese Line (CL); Sestri-Voltaggio Line (SVL); PF: Penninic Thrust Front. BAL = chrysotile asbestos Balangero mine (Province of Torino). The star indicates the recovery position of the studied sepiolite specimen, near Perletoa village.

Figure 2. Visual appearance of the Perletoa sepiolite: (a) thick bundles of fibres still attached to the serpentine substrate and (b) isolated. Notice how the fibrous habit is well evident even at the macroscopic scale.

Figure 3. Secondary electron SEM image showing several bundles of thinner fibrils orientated approximately in the same direction. The flexibility of the Perletoa sepiolite is evidenced by the accentuated bending shown by some fibres.

Figure 4. TEM micrographs of sepiolite fibres in cross section, observed along the [001] direction. At medium magnification the fibrils show a rhomboidal to parallelogram-like contour and quite a large open texture (a). At high magnification the incipient ‘opening’ process undergone by the central thick fibre, which causes subdivision in thinner units, can be better appreciated (split surfaces shown as dashed white lines). A roughly continuous and scarcely electron-dense film (possibly organic matter) surrounding the fibre contours and filling the interstices is indicated by arrows (b).

Figure 5. Simplified scheme of the ‘opening’ process which splits thick and elongated rhombic prismatic fibres into thinner ones. Preferential cleavage on the (110) crystal plane causes progressive fragmentation of a thicker sepiolite fibre (a) and consequent partition in some (4) thinner fibrils, maintaining the same rhomboidal contour and elongated in the [001] direction (b). Evolution of the same process causes the thinner fibrils to progressively get far from each other (c). The actual process, as a matter of fact, forms less regular smaller units. (100) and (010) faces, corresponding to minor cleavage planes, are also indicated for sake of clarity.

Figure 6: Observed TGA/derivative weight and heat flow/derivative heat flow curves for the Perletoa sepiolite. Vertical scale for the TGA curve is weight loss %.

Figure 7. FTIR spectra in the stretching region of the Perletoa sepiolite in air (1) and evacuated at room temperature (2), 120 °C (3) and 150 °C (4) respectively. Spectra are shifted on the Y axis for sake of clarity.

Figure 8. FTIR spectra in the bending region of the Perletoa sepiolite in air (1) and evacuated at room temperature (2), 120 °C (3) and 150 °C (4) respectively. Spectra are shifted on the Y axis for sake of clarity.

Figure 9. Observed (crosses) and calculated (solid line) patterns for the Rietveld refinement of the Perletoa sepiolite, together with the related difference (lower line).

Figure 10. Refined structure of the Perletoa sepiolite as resulting from the Rietveld procedure (crystal cell outlined in solid bars; H atoms arbitrarily added to both zeolitic H_2O and structural OH_2).

Figures

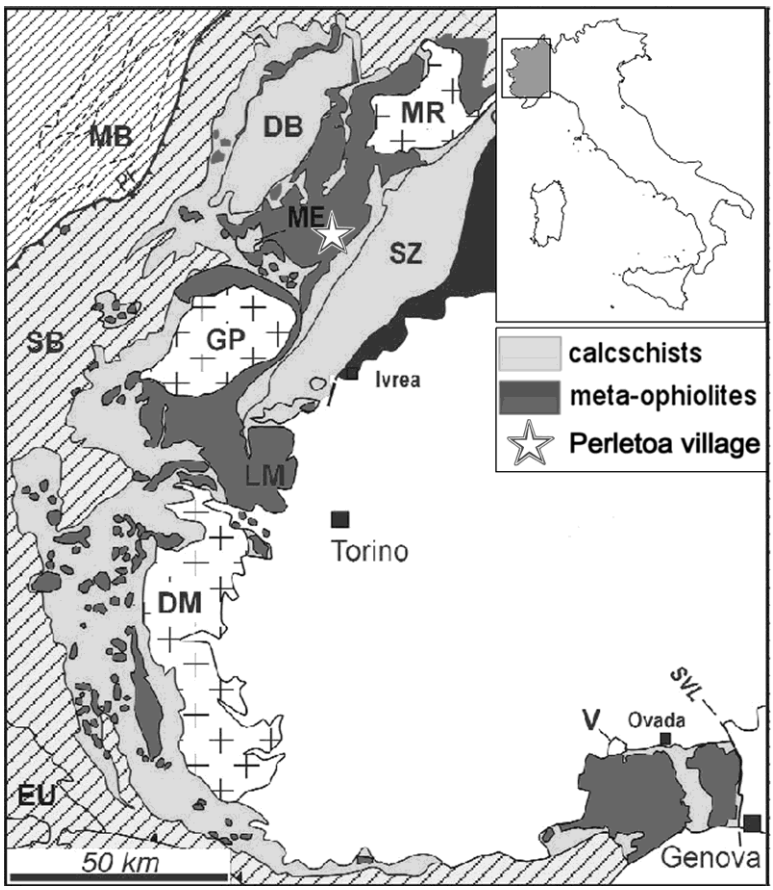

Fig. 1.

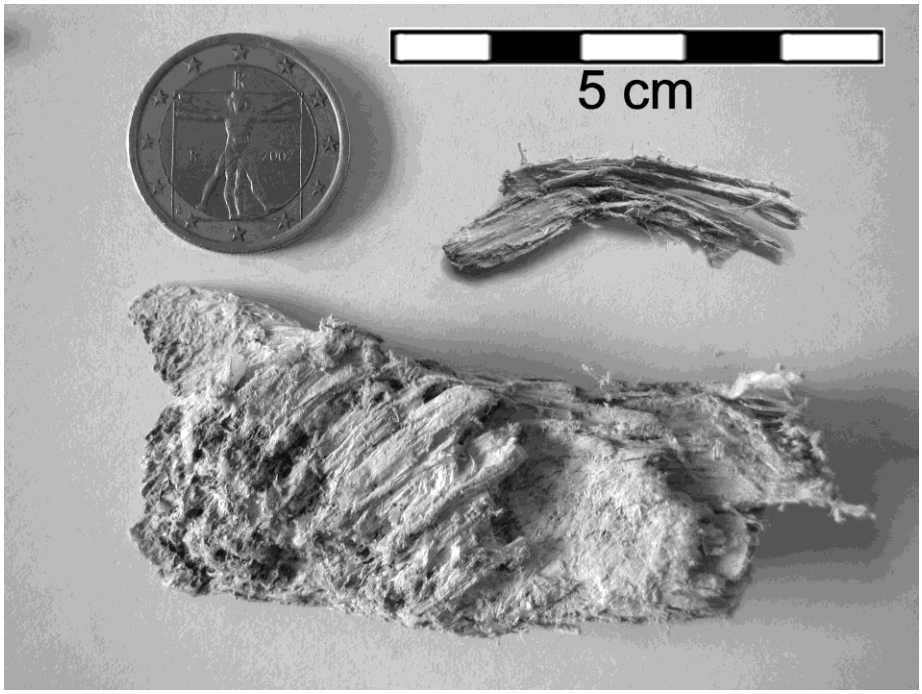

Fig. 2.

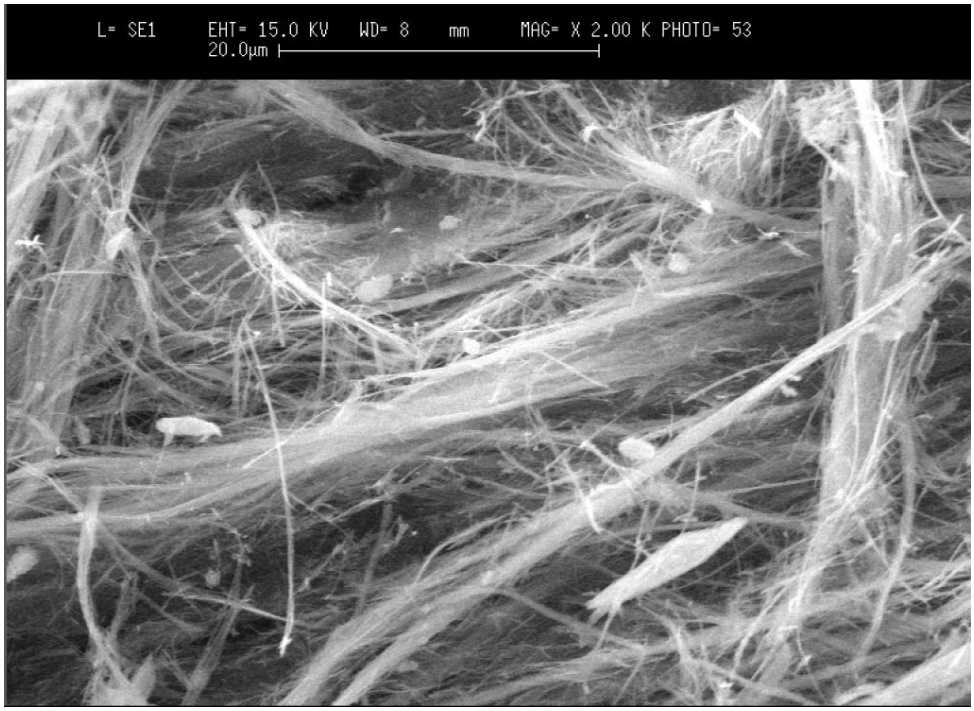
L= SE1 EHT= 15.0 KV WD= 8 mm MAG= X 2.00 K PHOTO= 53
20.0µm

Fig 3.

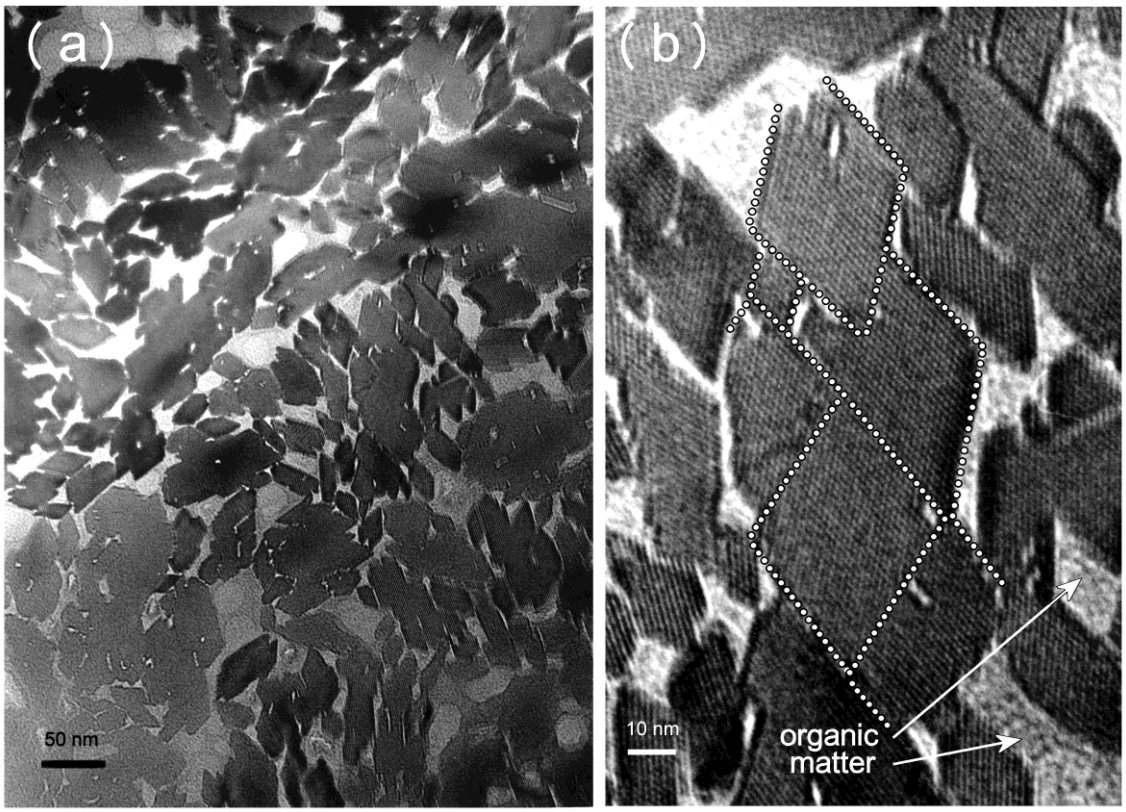
(a)
50 nm
(b)
10 nm
organic
matter

Fig. 4.

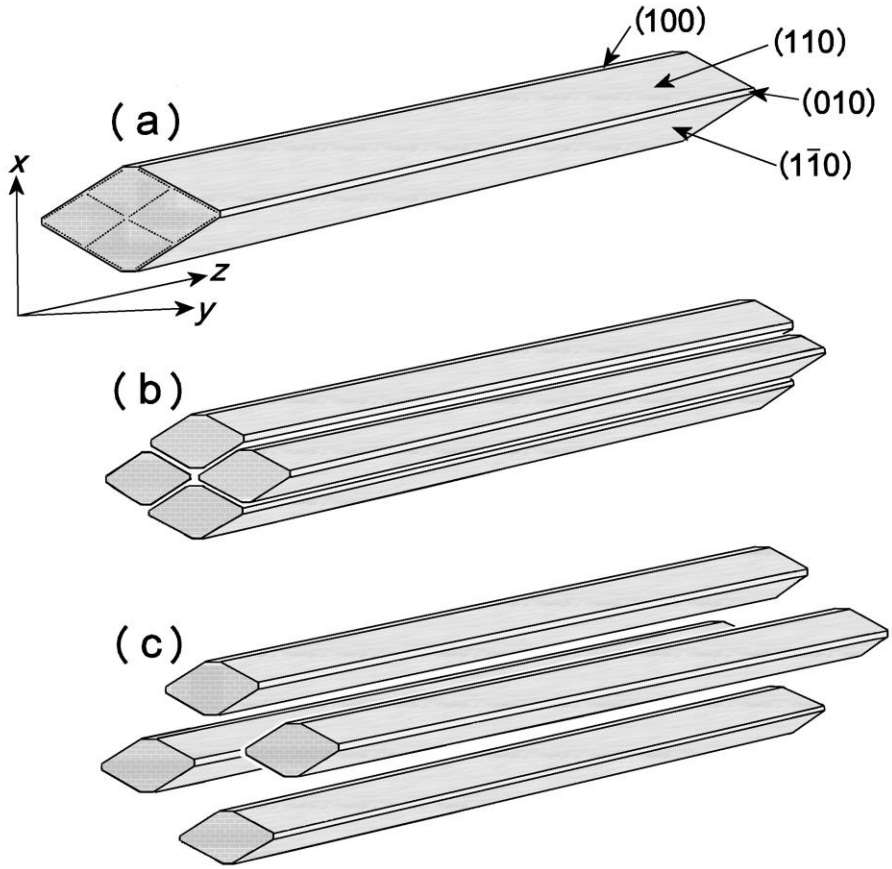
(100)
(110)
(010)
(1$\bar{1}$0)
(a)
x
z
y
(b)
(c)

Fig. 5.

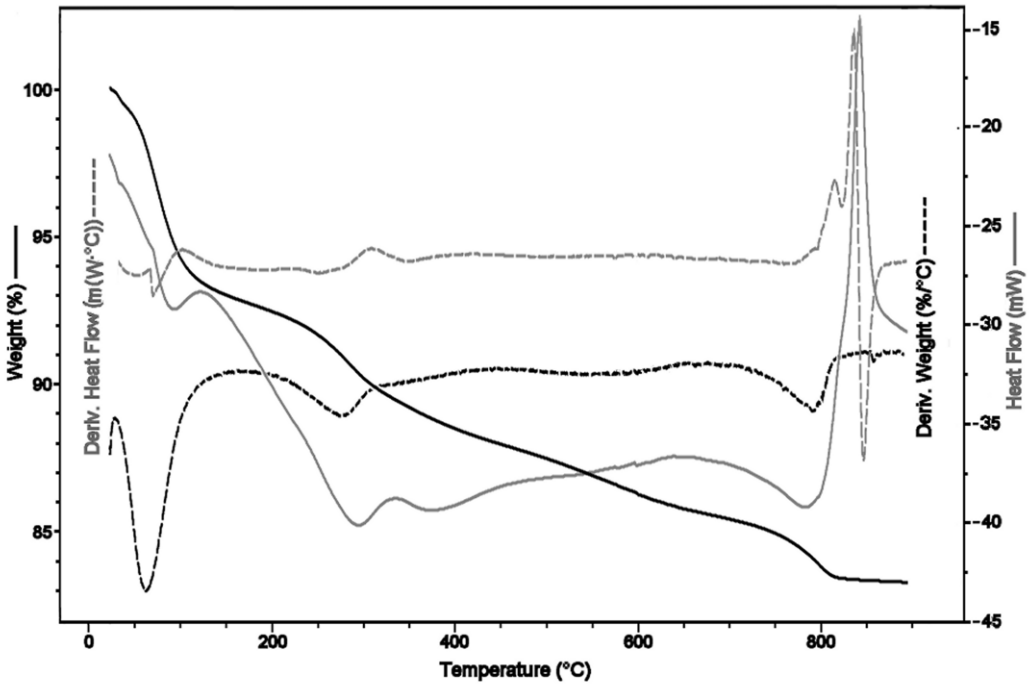
Weight (%)
Deriv. Heat Flow (mW/°C)
Deriv. Weight (%/°C)
Heat Flow (mW)
Temperature (°C)
100
95
90
85
0
200
400
600
800
-15
-20
-25
-30
-35
-40
-45

Fig. 6.

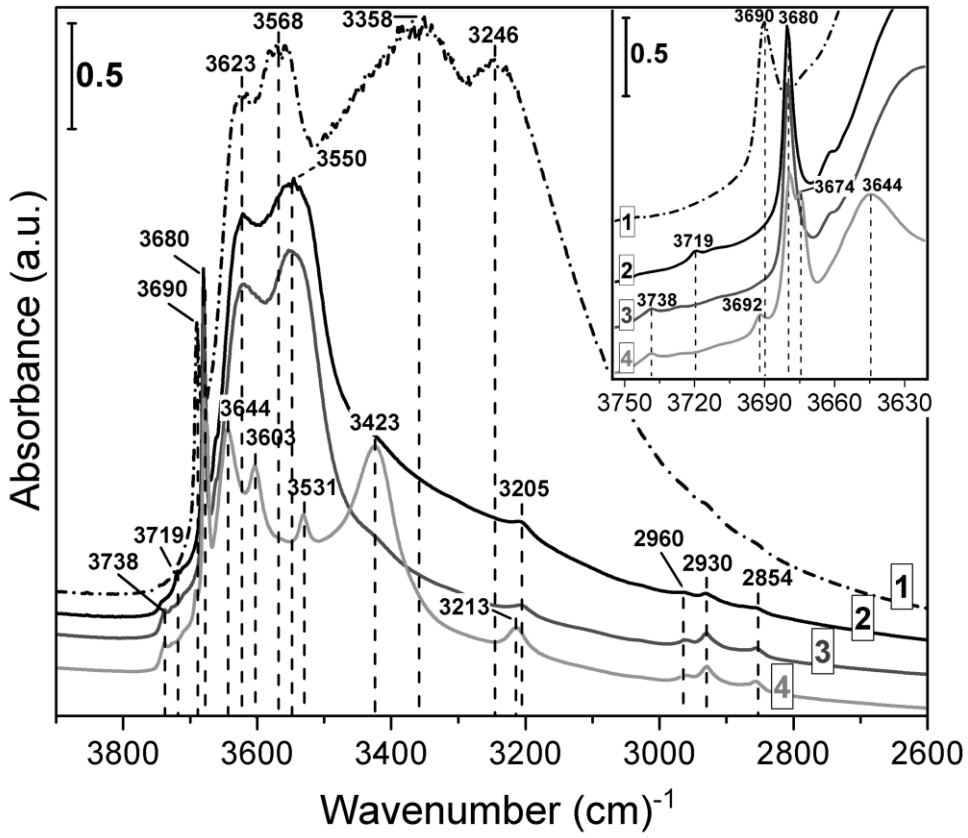
0.5
3568
3358
3246
3623
3550
3680
3690
3644
3603
3423
3531
3205
3719
3738
2960
2930
2854
3213
1
2
3
4
Absorbance (a.u.)
3800
3600
3400
3200
3000
2800
2600
Wavenumber (cm)-1
0.5
3690
3680
3674
3644
3719
3738
3692
3750
3720
3690
3660
3630

Fig. 7.

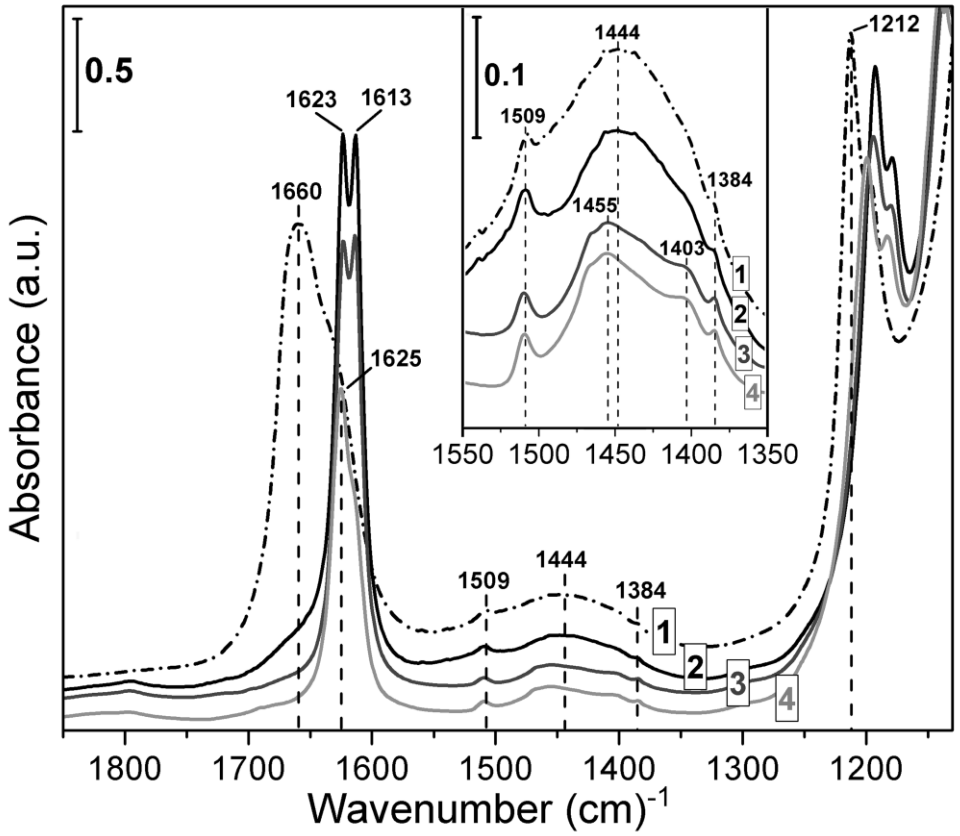
0.5
1623
1613
1660
1625
1509
1444
1384
1212
0.1
1455
1403
1
2
3
4
Absorbance (a.u.)
1800
1700
1600
1500
1400
1300
1200
Wavenumber (cm)-1
1550
1500
1450
1400
1350

Fig. 8.

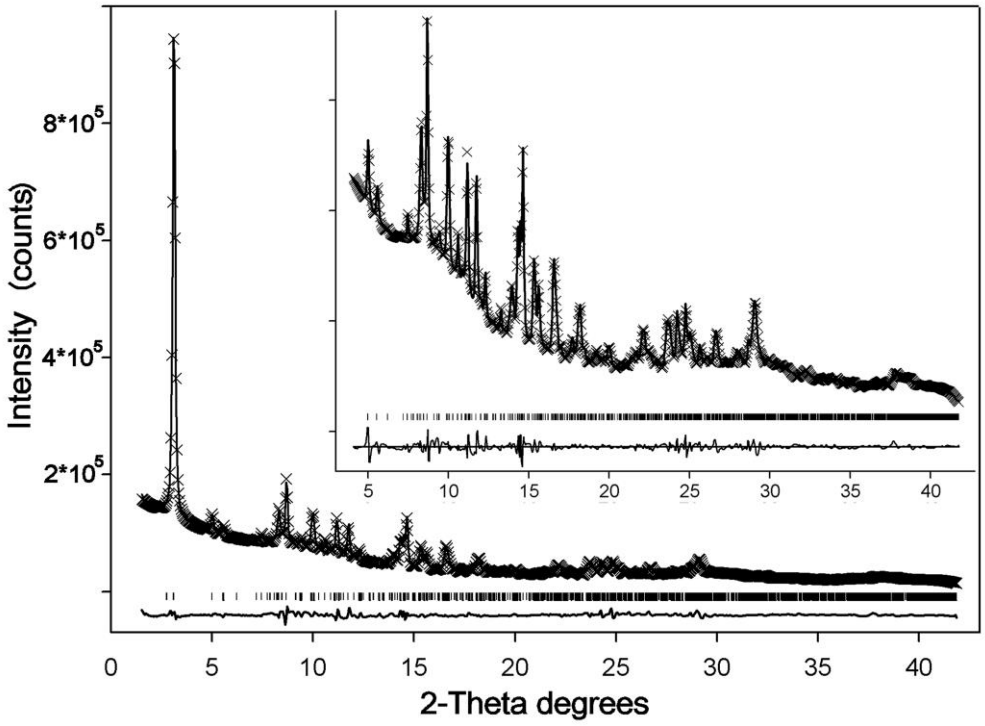
Intensity (counts)
8*10^5
6*10^5
4*10^5
2*10^5
0
5
10
15
20
25
30
35
40
2-Theta degrees

Fig. 9.

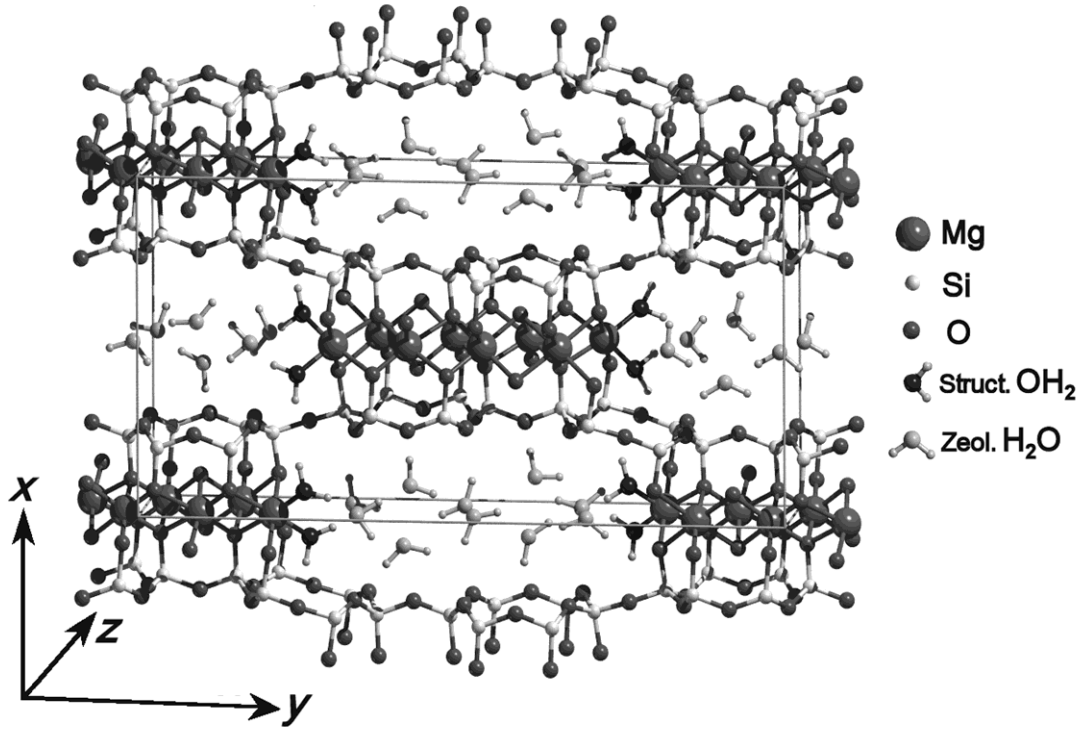
Mg
Si
O
Struct. OH2
Zeol. H2O
x
z
y

Fig. 10.